

Nonholonomic Virtual Constraints and Gait Optimization for Robust Walking Control

Journal Title
XX(X):1–24
©The Author(s) 2016
Reprints and permission:
sagepub.co.uk/journalsPermissions.nav
DOI: 10.1177/ToBeAssigned
www.sagepub.com/



Brent Griffin and Jessy Grizzle

Abstract

A key challenge in robotic bipedal locomotion is the design of feedback controllers that function well in the presence of uncertainty, in both the robot and its environment. This paper addresses the design of feedback controllers and periodic gaits that function well in the presence of modest terrain variation, without over reliance on perception and a priori knowledge of the environment. Model-based design methods are introduced and subsequently validated in simulation and experiment on MARLO, an underactuated three-dimensional bipedal robot that is roughly human size and is equipped with an IMU and joint encoders. Innovations include an optimization method that accounts for multiple types of disturbances and a feedback control design that enables continuous velocity-based posture regulation via nonholonomic virtual constraints. Using a single continuously-defined controller taken directly from optimization, MARLO traverses sloped sidewalks and parking lots, terrain covered with randomly thrown boards, and grass fields, all while maintaining average walking speeds between 0.9–0.98 m/s and setting a new precedent for walking efficiency in realistic environments.

Keywords

Bipedal robots, rough terrain, underactuated control, hybrid systems, virtual constraints.

1 Introduction

Humans and animals can walk over a variety of terrains without directly observing the ground. To be practical, bipedal robots must be able to do the same. In Buss et al. (2014, 2016), we achieved three-dimensional (3D) walking on flat-ground using holonomic virtual constraints and manually-designed walking gaits. In this paper, we extend our previous work by designing feedback controllers that allow a 3D bipedal robot to walk outdoors over sloped sidewalks, parking lots, and lawns and indoors over randomly placed planks, all without a priori knowledge of the environment or external sensing. Model-based design methods are introduced and subsequently validated in simulation and experiment on MARLO, a 3D bipedal robot with six actuators and thirteen DOF shown in Figure 1. The current results over uneven terrain are a consequence of using nonholonomic virtual constraints, which enable MARLO to adapt posture with velocity, and a walking gait optimization that accounts for uneven terrain and other disturbances. Using a controller taken directly from optimization, MARLO is able to traverse a variety of outdoor environments while maintaining a mechanical cost of transport (MCOT) between 0.67–0.69 and average walking speeds between 0.9–0.98 m/s. Videos of outdoor experiments are available at Dynamic Legged Locomotion Lab (2016).

1.1 Walking Gait Optimization

In this paper, the gait design problem is formulated in terms of parameter optimization, which uses a cost function that accounts for periodicity and efficiency under nominal walking conditions and additional terms that specifically

account for trajectory and control-effort deviations arising from a finite set of disturbances.

Numerous methodologies are being considered to quantify and improve the capacity of a bipedal robot to walk over uneven terrain. The terrain variations can be deterministic or random, and the control policy can involve switching or not. The gait sensitivity norm from Hobbelen and Wisse (2007, 2008b); Wisse et al. (2005) has been used to measure deviations in state trajectories arising from unknown *step decreases* in ground height. Swing-leg retraction, employed by bipedal animals, has been observed in Seyfarth et al. (2003) to be helpful in accommodating this class of disturbances. The mean-time to falling has been used in Byl and Tedrake (2009) to assess walking performance in the presence of *stochastic ground height variations*. For low-dimensional dynamical systems, such as the rimless wheel and the compass-gait bipedal walker, numerical dynamic programming has been used to maximize the mean time to falling. The simultaneous design of a periodic walking gait and a linear time-varying controller that minimizes deviations induced by ground height changes is addressed in Dai and Tedrake (2012, 2013). The results are illustrated through simulation on the compass-gait biped and on Rabbit, a five-link biped with knees. A time-invariant linear controller that is robust to modest terrain variations

Department of Electrical Engineering and Computer Science, University of Michigan, USA

Corresponding author:

Brent Griffin, Department of Electrical Engineering and Computer Science, University of Michigan, Ann Arbor, MI 48109 USA.
Email: griffb@umich.edu



Figure 1. MARLO, an ATRIAS 2.1 robot designed by the Dynamic Robotics Laboratory at Oregon State University, is able to traverse man-made (top) and natural (bottom) terrain using a single continuously-defined controller based on the mathematical model of the robot. The mobile gantry does not provide any stabilization or support during walking.

is developed in Manchester et al. (2011), using transverse linearization and a receding-horizon control framework; experiments are performed on a compass-gait walker. An event-based controller is given in Kolathaya and Ames (2012) that updates parameters in a fixed controller in order to achieve a *dead-beat control response*, in the sense that after a terrain disturbance, it steers the robot's state back to its value at the end of the nominal periodic gait. A control architecture that *switches among a finite-set of controllers* when dealing with terrain variation is studied in Yang et al. (2009); Park et al. (2013); Manchester and Umenberger (2014); Saglam and Byl (2014b).

In this paper, we seek a single (non-switching) controller and nominal periodic gait that are insensitive to a predetermined and finite set of terrain and velocity variations. The choice of a single controller is motivated in part by ease of implementation, but even in the context of a switching controller, it seems desirable that one of the controllers be insensitive to a pre-determined range of terrain and velocity variations.

Motivated by the approach of Dai and Tedrake (2012, 2013), we seek a periodic walking gait that can accommodate a finite set of perturbations in ground height. Additionally,

we introduce a finite set of perturbations to velocity, which is shown to improve performance for repeated disturbances. Trajectory and control deviations induced by the perturbations are defined with respect to a nominal periodic orbit via a gait phasing variable. As in Westervelt et al. (2007), a parameterized family of *nonlinear controllers* is assumed to be known, and constrained parameter optimization is used to select a periodic solution of the closed-loop system that satisfies limits on torque, ground reaction forces, and other physical quantities. Motivated by Dai and Tedrake (2012, 2013), the cost function is augmented with terms that penalize deviations in the state and control trajectories arising from perturbations. The gait phasing variable is used to penalize more heavily deviations that persist “late” into the gait, which is shown in Griffin and Grizzle (2015b) to improve the ability of a planar robot to handle terrain deviations, both in simulation and in experiments.

1.2 Nonholonomic Outputs

Virtual *holonomic* constraints are functional relations among the configuration variables of a robot that are dynamically imposed through feedback control. Their purpose is to

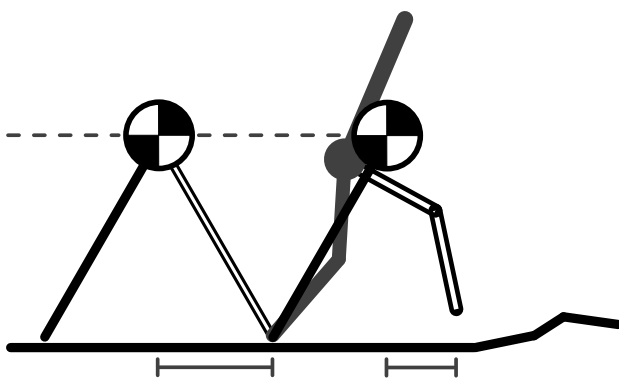


Figure 2. Velocity-based swing foot placement has been designed on the basis of the linear inverted pendulum model in Pratt and Tedrake (2006). Using nonholonomic outputs, it is possible to implement velocity-based posture regulation that accounts for the full dynamics of the biped, as well as a range of terrain variation.

synchronize the evolution of the various links to an internal *gait phasing* or *gait timing variable*, such as the position of the robot's hip with respect to the stance leg end. The gait timing variable is selected to be monotonically increasing along a walking motion so that it can replace time as a means to parameterize command "trajectories." From a theoretical perspective, virtual constraints turn the Isidori-Byrnes theory of nonlinear zero dynamics from Isidori (1995) into a formal gait and feedback design tool, while the experiments reported in Westervelt et al. (2004); Park et al. (2013); Buss et al. (2014); Zhao et al. (2014); Martin et al. (2014a); Gregg et al. (2014a) attest to the applicability of the approach to realize dynamic locomotion that meets a range of design objectives, from speed of locomotion, to limits on actuator torque, and available friction cone, to name only a few.

This paper introduces a more general class of *nonholonomic* outputs that depend on velocity. The motivation for this extension comes from the work of Pratt and Tedrake (2006), which plans the desired placement of a biped's swing foot as a function of the center of mass velocity in the horizontal direction. Their control law for foot placement is based on the linear inverted pendulum model (aka LIP) proposed in Kajita et al. (1992), which approximates the robot's dynamics as an inverted pendulum with constant vertical height and massless legs, as shown in Figure 2. Due to the assumptions of constant vertical height and massless legs, the pendulum's dynamic model is linear, the reset map associated with leg impact is linear and energy conserving, and the overall hybrid model can be solved in closed form. From the closed-form solution of the LIP model, Pratt and Tedrake (2006); Koolen et al. (2012) propose a foot placement policy to regulate forward walking speed, and have illustrated it on complex robots, such as a simulation model of the M2V2 biped undergoing impulses of up to 15 Ns in Pratt et al. (2012). Similar adjustments are made heuristically to step length and torso pitch in Post and Schmiedeler (2014) to improve velocity stabilization of the planar biped ERNIE.

In this paper, a continuous velocity-dependent posture-regulating strategy is designed and implemented without relying on an inverted pendulum approximation of the robot.

In particular, the distributed mass, multi-link nature of the robot can be fully taken into account, including energy losses at impact. The control law is implemented through a set of virtual constraints that depend on velocity through generalized conjugate momenta, in addition to the robot's configuration variables. A set of parameterized splines appearing in the virtual constraints are designed through the parameter optimization process introduced in Section 1.1. The robustness of the resulting control solutions to terrain and velocity perturbations are evaluated through simulation and experiments. Control solutions based on *nonholonomic constraints* accommodate a wider range of perturbations than those based on *holonomic constraints*.

1.3 Contributions and Organization

This paper is the culmination of work initiated for planar walking studies in the conference papers Griffin and Grizzle (2015a,b).

With respect to prior work on accommodating unknown terrain variations, the primary contributions include: allowing a family of nonlinear controllers to be optimized with respect to disturbance attenuation; introducing a finite set of perturbations to velocity during control optimization and demonstrating efficacy; synchronizing the calculation of trajectory and control deviations of a biped's gait via a gait phasing variable; and penalizing more heavily trajectory deviations that persist late into a step, when ground contact is likely to occur.

With respect to prior work with virtual constraints, the primary contributions include: introducing a new class of virtual constraints that include velocity, but maintain control outputs that are relative degree two for ease of implementation; and demonstrating superior ability to attenuate terrain and velocity perturbations.

With respect to prior work on feedback control of bipedal robots, the primary contributions are: introducing a model-based design framework that is able to achieve dynamic three-dimensional walking without hand-tuning of the optimized walking gait; demonstrating robustness by traversing sloped sidewalks and parking lots, terrain covered with randomly thrown boards, and grass fields without a priori knowledge of the environment or external sensing (the robot uses only an IMU and joint encoders); and setting a new precedent by evaluating walking efficiency for a variety of realistic terrains.

The remainder of this paper is organized as follows. Section 2 describes the hybrid model of walking used in this paper. Section 3 presents a parameter-optimization-based control design method for accommodation of unknown disturbances, and Section 4 presents the notion of relative degree two nonholonomic outputs. Section 5 details a specific implementation of the general concepts introduced in this paper. To demonstrate the efficacy of new concepts and establish best practices, Section 6 compares simulation results for many different control solutions. Each control solution results from a unique design configuration selected explicitly for this purpose. Section 7 gives the results of robot experiments using control solutions designed for outdoor environments, with corresponding discussion given at the end of the section. Finally, Section 8 provides concluding remarks.

2 Walking Model and Solutions

2.1 Hybrid Model

The walking model assumes alternating phases of single support (one foot on the ground) and double support (both feet in contact with the ground). The single support phase assumes the stance foot is not slipping and evolves as a passive pivot. The standard robot equations apply and give a second order model that is expressed in state variable form

$$\dot{x} = f(x) + g(x)u, \quad (1)$$

where $x \in \mathcal{X}$ is the state of the system and $u \in R^m$ are the control inputs. For later use, a parameterized family of continuous-time feedbacks is assumed to be given

$$u = \Gamma(x, \beta), \quad (2)$$

where $\beta \in \mathcal{B}$ are control parameters from an admissible set. The resulting closed-loop system is

$$\dot{x} = f^{cl}(x, \beta) := f(x) + g(x)\Gamma(x, \beta). \quad (3)$$

The closed-loop system is assumed to be continuously differentiable in x and β , thereby guaranteeing local existence and uniqueness of solutions.

With the stance foot taken as the origin, let p_2 be the Cartesian position of the swing foot on the second leg, and denote by p_2^v its vertical component. The double support phase occurs when the swing foot strikes the ground which is modeled as

$$p_2^v(x) - d = 0, \quad (4)$$

for $d \in D$, a finite collection of ground heights used to account for varying terrain. It will be assumed at impact that the transversality condition $\dot{p}_2^v(x) < 0$ is met. Physically, it corresponds to the impact occurring at a point in the gait where the swing foot is moving down toward the ground, as opposed to the impact occurring early in the gait which would lead to tripping Park et al. (2013). The impact is modeled as a collision of rigid bodies using the model of Hürmüzlü and Marghitu (1994). Consequently, the impact is instantaneous and gives rise to a continuously-differentiable reset map

$$x^+ = \Delta(x^-), \quad (5)$$

that does not depend on the ground height since the vector of pre-impact states, x^- , provides foot height at impact. Here, x^+ is the vector of the post-impact states. So that only one continuous-phase mechanical model is needed, the impact map is assumed to include leg swapping, as in (Westervelt et al. 2007, pp. 57). Moreover, for reasons that will become clear in Section 5.2, the impact map is allowed to depend on β .

The overall hybrid model is written as

$$\Sigma : \begin{cases} \dot{x} = f^{cl}(x, \beta) & x^- \notin \mathcal{S}^d \\ x^+ = \Delta(x^-, \beta) & x^- \in \mathcal{S}^d \end{cases}, \quad (6)$$

where

$$d \in D := \{d_0, d_1, \dots, d_{N_d}\} \quad (7)$$

is the set of ground height variations and

$$\mathcal{S}^d := \{x \in \mathcal{X} \mid p_2^v(x) - d = 0, \dot{p}_2^v(x) < 0\} \quad (8)$$

is the hypersurface in the state space where the swing leg impact occurs at ground height $d \in D$.

Remark: The reference (Westervelt et al. 2007, pp. 109) shows how to augment the state variables with control parameters in order to accommodate event-based control, as used in Kolathaya and Ames (2012). This extension is employed later in (64).

2.2 Model Solutions

For a given value of $\beta \in \mathcal{B}$, a solution of the hybrid model (6) is defined by piecing together solutions of the differential equation (3) and the reset map (5); see (Westervelt et al. 2007, pp. 56); Hürmüzlü and Marghitu (1994). We are interested in periodic orbits and their perturbations and exclude Zeno and other complex behavior from our notion of a solution.

In the following, for compactness of notation, explicit dependence on β is dropped. A *step* of the robot starts at time t_0 with $x_0 \in \mathcal{S}^{\bar{d}_0}$ for a given value of $\bar{d}_0 \in D$. The reset map is applied, giving an initial condition $\Delta(x_0)$ for the ODE (3), with solution $\varphi(t, t_0, \Delta(x_0))$. The step is completed if the solution of the ODE can be continued until a (first) time $t_1 > t_0$ when $x_1 = \varphi(t_1, t_0, \Delta(x_0)) \in \mathcal{S}^{\bar{d}_1}$ for a given value of $\bar{d}_1 \in D$. Not all steps can be completed, but when one is completed, the next step begins by solving the ODE with initial condition $\Delta(x_1)$ at time t_1 , etc. The solution (or step) is *periodic* if $\varphi(t_1, t_0, \Delta(x_0)) = x_0$, and $T = t_1 - t_0$ is the *period*. Because the model is time invariant, wherever convenient, the initial time is taken as $t_0 = 0$ and the solution denoted as $\varphi(t, \Delta(x_0))$.

3 Optimization for the Accommodation of Unknown Disturbances

3.1 Terrain Disturbances

Let $d_0 \in D$ represent the nominal change in ground height *step to step*. We seek $\beta \in \mathcal{B}$ and $x_0 \in \mathcal{X}$ giving rise to a periodic solution of the closed-loop system (6); that is, for which there exists $T_0 > 0$ such that

$$x_0 = \varphi(T_0, \Delta(x_0)). \quad (9)$$

Moreover, for the same value of $\beta \in \mathcal{B}$, we desire that the periodic orbit ensures the existence of the following additional solutions of the closed-loop system: $\forall 1 \leq i \leq N_d, d_i \in D, 1 \leq j \leq N_s, \exists 0 < t_i < \infty$ and $0 < T_{ij} < \infty$ such that

$$x_{i1} = \varphi(t_i, \Delta(x_0)) \in \mathcal{S}^{d_i} \quad (10)$$

$$x_{i(j+1)} = \varphi(T_{ij}, \Delta(x_{ij})) \in \mathcal{S}^{d_0}. \quad (11)$$

In plain words, there exist steps that begin on the periodic orbit, end at ground height d_i , and continue for at least N_s more steps at nominal ground height d_0 , as shown in Figure 3.

In the following, we set up a parameter optimization problem in (β, x_0) for finding a periodic solution that meets these conditions. Moreover, we will pose a cost function on the steps following the change in ground height that favors solutions that “return closely” to the nominal periodic solution, that is, the closed-loop system attenuates the effects of the set of ground height variations.

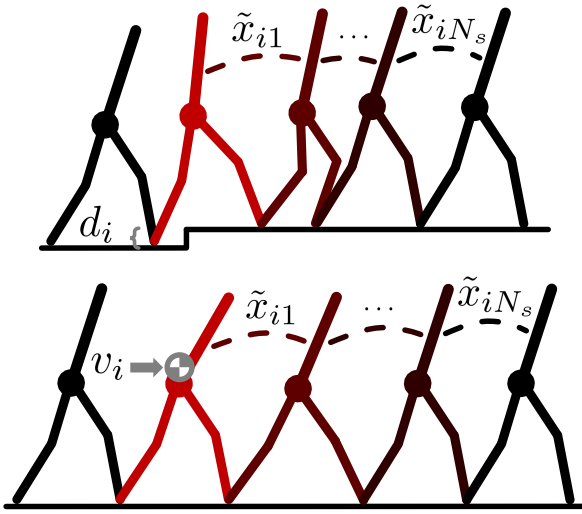


Figure 3. Terrain (top) and velocity (bottom) disturbances for optimization. Data are collected for N_s steps following a perturbation caused by d_i or v_i . \tilde{x}_{ij} represents the perturbed state trajectory of the j th step following disturbance i .

3.2 Velocity Disturbances

The method of Section 3.1 can accommodate a variety of disturbances. Here, velocity disturbances are addressed. Let $x_{v_0} \in \mathcal{X}$ represent the values of the state in the periodic orbit when the position of the center of mass is directly above the stance foot in the sagittal plane. Given a set of Cartesian velocity variations for the center of mass,

$$v \in V := \{v_1, v_2, \dots, v_{N_v}\}, \quad (12)$$

where $v \in \mathbb{R}^3$, define the i th velocity perturbation as

$$x_{v_i} := x_{v_0} + \delta x_{v_i}, \quad (13)$$

such that $p_{cm}(x_{v_i}) = p_{cm}(x_{v_0})$ and

$$v_i = \frac{\partial p_{cm}(x_{v_0})}{\partial x} \delta x_{v_i}, \quad (14)$$

where $p_{cm}(x)$ gives the Cartesian position of the center of mass corresponding to x .

For the purpose of attenuating the effects of velocity variations, we desire that the periodic orbit ensures the existence of the following additional solutions of the closed loop system: $\forall 1 \leq i \leq N_v, v_i \in V, 1 \leq j \leq N_s, \exists 0 < t_i < \infty$ and $0 < T_{ij} < \infty$ such that

$$x_{i1} = \varphi(t_i, x_{v_i}) \in \mathcal{S}^{d_0} \quad (15)$$

and $x_{i(j+1)} = \varphi(T_{ij}, \Delta(x_{ij})) \in \mathcal{S}^{d_0}$, as in (11). In plain words, there exist steps that begin on the periodic orbit, end at nominal ground height d_0 after a velocity disturbance v_i is applied mid-step, and continue for at least N_s more steps at nominal ground height d_0 , as shown in Figure 3.

Remarks: (a) When applying multiple disturbance types, the index i in (11) must be offset for each type of disturbance for calculations in Section 3.3. (b) We found that applying a velocity perturbation in the middle of a step is beneficial for finding solutions that satisfy the conditions in (15), while allowing time for the controller to make adjustments before the end of the step. It is possible, however, to apply a velocity disturbance at any point along the periodic orbit.

3.3 Gait Phase and Trajectory Deviations

Compared to time-based methods, phase-based synchronization of walking trajectories is shown to be more natural to humans in Gregg et al. (2014b) and advantageous for control in Kong et al. (2015). For this optimization method, we have found that computing deviations of the perturbed solutions from the nominal periodic solution does not work well when the trajectories are parameterized by time. This is because terrain disturbances cause varying initial conditions, which cause perturbed trajectories to be unsynchronized with respect to time. We use instead a *gait phasing variable*, $\bar{\tau} : \mathcal{X} \rightarrow \mathbb{R}$, that is strictly increasing along walking steps. Examples include the angle of the line connecting the hip and the ground contact point of the stance leg, the horizontal position of the center of mass, or the horizontal position of the hips, which will be used in Section 5. The gait phase can be thought of as a measure of progress through each step. We further assume that the units are normalized on the periodic orbit so that it takes values in $[0, 1]$, namely

$$\bar{\tau}(\Delta(x_0)) = 0 \quad (16)$$

$$\bar{\tau}(x_0) = 1, \quad (17)$$

and that $L_g \bar{\tau}(x) := \frac{\partial \bar{\tau}}{\partial x}(x) g(x) = 0$.

Let $\bar{\tau}_{ij}(t) := \bar{\tau}(\varphi(t, \Delta(x_{ij})))$, for $0 \leq t \leq T_{ij}$, and as in Dai and Tedrake (2012), denote by τ_{ij}^+ and τ_{ij}^- the initial and final values of $\bar{\tau}$ along the trajectory. Due to the assumption that $\bar{\tau}_{ij}$ is strictly increasing, the inverse map $\bar{\tau}_{ij}^{-1} : [\tau_{ij}^+, \tau_{ij}^-] \rightarrow [0, T_{ij}]$ exists. Define

$$\tilde{x}_{ij}(\tau) := \varphi(\bar{\tau}_{ij}^{-1}(\tau), \Delta(x_{ij})) \quad (18)$$

$$\tilde{u}_{ij}(\tau) := \Gamma(\varphi(\bar{\tau}_{ij}^{-1}(\tau), \Delta(x_{ij})), \beta). \quad (19)$$

For $1 \leq i \leq (N_d + N_v)$ and $1 \leq j \leq N_s$, deviations in the state and control trajectories are defined as

$$\delta x_{ij}(\tau) := \begin{cases} \tilde{x}_{ij}(\tau) - \tilde{x}_0(0) & \text{if } \tau < 0 \\ \tilde{x}_{ij}(\tau) - \tilde{x}_0(\tau) & \text{if } \tau \in [0, 1] \\ \tilde{x}_{ij}(\tau) - \tilde{x}_{0,\text{ext}}(\tau) & \text{if } \tau > 1 \end{cases} \quad (20)$$

$$\delta u_{ij}(\tau) := \begin{cases} \tilde{u}_{ij}(\tau) - \tilde{u}_0(0) & \text{if } \tau < 0 \\ \tilde{u}_{ij}(\tau) - \tilde{u}_0(\tau) & \text{if } \tau \in [0, 1] \\ \tilde{u}_{ij}(\tau) - \tilde{u}_{0,\text{ext}}(\tau) & \text{if } \tau > 1 \end{cases} \quad (21)$$

for $\tau_{ij}^+ \leq \tau \leq \tau_{ij}^-$, where $\tilde{x}_{0,\text{ext}}(\tau)$ and $\tilde{u}_{0,\text{ext}}(\tau)$ are forward extensions of the nominal periodic trajectories.¹

Using (20) and (21), the weighted square error is defined as

$$\|\delta x_{ij}(\tau)\|^2 := \langle Q \delta x_{ij}(\tau), \delta x_{ij}(\tau) \rangle \quad (22)$$

$$\|\delta u_{ij}(\tau)\|^2 := \langle R \delta u_{ij}(\tau), \delta u_{ij}(\tau) \rangle \quad (23)$$

for Q and R positive semi-definite (constant) matrices.

3.4 Robust Control Cost Function

The problem of defining a cost function \mathcal{J}_0 and appropriate equality and inequality constraints for determining a nominal periodic solution of (3) has been addressed in (Westervelt et al. 2007, pp. 151-155); Westervelt et al. (2004); Sreenath

et al. (2011) using parameter optimization. Here, we define additional terms that penalize deviations induced by the terrain-height disturbances in D and velocity disturbances in V .

For $1 \leq i \leq (N_d + N_v)$ and $1 \leq j \leq N_s$, we define

$$\mathcal{J}_{ij} :=$$

$$\frac{1}{(\tau_{ij}^- - \tau_{ij}^+)^2} \int_{\tau_{ij}^+}^{\tau_{ij}^-} (\tau - \tau_{ij}^+) (\|\delta x_{ij}(\tau)\|^2 + \|\delta u_{ij}(\tau)\|^2) d\tau. \quad (24)$$

The term $\frac{(\tau - \tau_{ij}^+)}{(\tau_{ij}^- - \tau_{ij}^+)}$ scales the errors so that initial deviations from the nominal periodic trajectory are discounted with respect to errors toward the end of the step. The rationale for this is that if the closed-loop system were to rejoin the nominal periodic orbit by the end of the step, the disturbance would have been rejected and a next step would be guaranteed. The scale factor allows the optimization to focus on approximately achieving this objective. The benefit of the scale factor introduced in (24) is demonstrated in Griffin and Grizzle (2015b) by comparing optimization solutions that include the scale factor against those that do not. The additional term outside the integral, $\frac{1}{(\tau_{ij}^- - \tau_{ij}^+)}$, is included so that perturbed step costs are normalized w.r.t. the varying ranges of τ_{ij} that result from disturbances (e.g., higher and lower terrain).

The overall cost function is

$$\mathcal{J} = \mathcal{J}_0 + \sum_{i=1}^{N_d+N_v} \sum_{j=1}^{N_s} w_{ij} \mathcal{J}_{ij}, \quad (25)$$

where w_{ij} determines the relative weight of each step.

Parameter optimization problem: Find $(\beta; x_0)$ that (locally) minimize \mathcal{J} subject to the existence of a periodic solution of (6) that respects ground contact conditions, torque limits, and other relevant physical properties, as illustrated in Section 5.3.

4 Relative Degree Two Nonholonomic Outputs

Assume an n -degree of freedom mechanical model

$$D(q)\ddot{q} + C(q, \dot{q})\dot{q} + G(q) = Bu, \quad (26)$$

with m actuators and Lagrangian

$$\mathcal{L}(q, \dot{q}) := \frac{1}{2} \dot{q}^\top D(q)\dot{q} - V(q). \quad (27)$$

Assume moreover that the configuration variables $q = (q_u, q_a)'$ have been selected such that $q_u = (q_1, \dots, q_{(n-m)})'$ are unactuated and $q_a = (q_{(n-m+1)}, \dots, q_n)'$ are actuated, so that, by Lagrange's equation,

$$\frac{d}{dt} \frac{\partial \mathcal{L}}{\partial \dot{q}_u} - \frac{\partial \mathcal{L}}{\partial q_u} = 0. \quad (28)$$

The quantity

$$\sigma := \frac{\partial \mathcal{L}}{\partial \dot{q}_u}(q, \dot{q}) \quad (29)$$

is the *momenta conjugate to q_u* , and for $1 \leq i \leq (n-m)$, is equal to

$$\sigma_i = D_i(q)\dot{q}, \quad (30)$$

where $D_i(q)$ is the i -th row of the mass-inertia matrix. From (28) and (29),

$$\frac{d}{dt} \sigma = \frac{\partial \mathcal{L}}{\partial q_u}(q, \dot{q}), \quad (31)$$

and thus if σ has a relative degree, it is two or greater. Indeed, differentiating σ a second time gives terms that depend on acceleration, which, via (26), may in turn depend on the input torque.

Functional relations involving *momenta* are classic examples of *nonholonomic constraints* Bloch (2003). Consider now a nonholonomic output function of the form

$$y = h(q, \sigma) \quad (32)$$

$$=: \tilde{h}(q, \dot{q}). \quad (33)$$

Then from the chain rule, its derivative along trajectories of the model is

$$\begin{aligned} \dot{y} &= \frac{\partial h(q, \sigma)}{\partial q} \dot{q} + \frac{\partial h(q, \sigma)}{\partial \sigma} \dot{\sigma} \\ &= \frac{\partial h(q, \sigma)}{\partial q} \dot{q} + \frac{\partial h(q, \sigma)}{\partial \sigma} \frac{\partial \mathcal{L}}{\partial q_u}(q, \dot{q}) \end{aligned} \quad (34)$$

and thus the relative degree cannot be less than two.

Remark: Equation (34) holds for one or more degrees of underactuation. Thus, it can be applied to both planar and 3D biped models, as well as models with or without compliant elements.

5 Control Design

This section provides an example implementation of the gait optimization method from Section 3 and the nonholonomic outputs from Section 4. Section 5.1 describes the bipedal robot and corresponding model. Section 5.2 defines the feedback control used for walking. Section 5.3 describes the optimization configuration for finding walking control solutions.

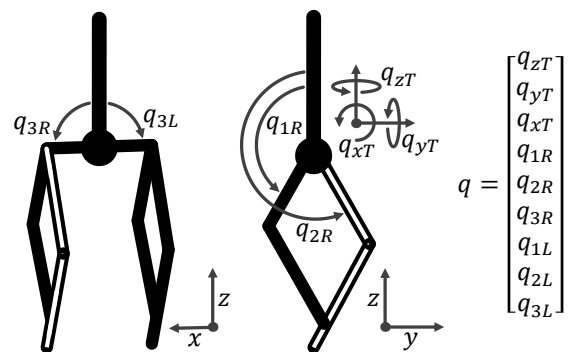


Figure 4. Rigid model of MARLO for control design and simulation. L and R designate left and right legs. q_{zT} , q_{yT} , and q_{xT} are the respective torso yaw, roll, and pitch Euler angles w.r.t. the world frame.



Figure 5. Two-contact-point feet (left) and prosthetic feet (right).

5.1 Bipedal Robot Model

The robot MARLO, shown in Figure 1, is the Michigan copy of the ATRIAS-series of robots built by Jonathan Hurst and is described in detail in Grimes and Hurst (2012); Ramezani et al. (2014). The robot's mass is approximately 55 kg and its legs are one meter long. Furthermore, while the robot has series elastic actuators, the springs used in this study are sufficiently stiff that they are ignored. Excluding the global Cartesian position, the resulting rigid model has nine DOF in single support and six actuators. Four sagittal-plane leg motors use harmonic drives with a 50:1 gear ratio, and two hip-abduction motors use a belt transmission with a 26.7:1 gear ratio. The power amplifiers for the leg and hip motors generate up to 5 Nm and 3 Nm of torque respectively.

The configuration variables $q = (q_u, q_a)'$ are shown in Figure 4. Specifically, the unactuated components are

$$q_u = [q_{zT}, q_{yT}, q_{xT}]', \quad (35)$$

and the actuated components are

$$q_a = [q_{1R}, q_{2R}, q_{3R}, q_{1L}, q_{2L}, q_{3L}]'. \quad (36)$$

With this choice of configuration variables, σ has three components corresponding to the angular momenta about the stance foot end in the yz -, xz -, and xy -planes (i.e., the sagittal, frontal, and transverse planes respectively). Because the model is 3D, the σ components can also be defined using x -, y -, and z -axes.

The complete hybrid model of the robot, including the dynamic model for the single support phase and the reset map at leg impact, is derived as in Ramezani et al. (2014), except yaw damping friction about the stance foot has been removed. Thus, the resulting walking gait is not dependent on yaw damping, which is beneficial for handling uncertain physical ground contact conditions during experiments with MARLO. Using the natural state variables $x = (q, \dot{q})'$, the Lagrange model (26) is expressed in state variable form as in (1), with $x \in \mathcal{X}$ an open subset of \mathbb{R}^{18} and $u \in \mathbb{R}^6$ for three degrees of underactuation during single support. Full details of the impact surface (8) and the reset map (5) are in Westervelt et al. (2007).

The robot model is assumed to be symmetric as in Hamed and Grizzle (2014). Hence, the control definition assumes right stance. During left stance, a coordinate transform on x maps the state of the robot to “right stance,” and the resulting “right-stance” control inputs are then mapped back to the actual left-stance control inputs.

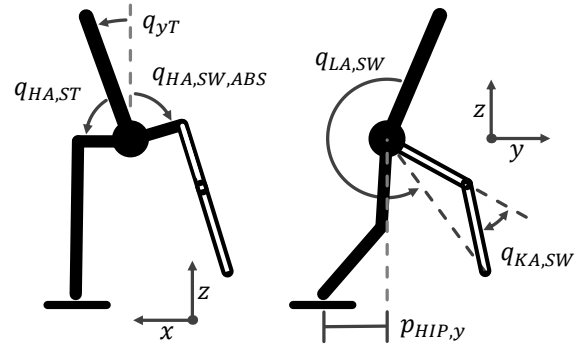


Figure 6. Controlled outputs and gait phasing variable. Control trajectories are synchronized with the motion of $p_{HIP,y}$.

For control calculation, the y -axis is attached to the forward direction of the torso; thus, despite yaw motion about the stance foot in simulation and experiments, control is yaw independent.² During experiments with MARLO, yaw motion is reduced by yaw friction from the two-contact-point feet shown in Figure 5. With these feet, MARLO pivots freely in the roll and pitch directions, which is consistent with the robot model. Some outdoor experiments use the prosthetic feet shown in Figure 5. Although prosthetic feet do not pivot as easily for roll and pitch, they provide a larger surface area for walking on compliant terrain, such as un-mowed grass.

5.2 Family of Feedback Controllers

The feedback controller is designed using the method of *virtual constraints* and *hybrid zero dynamics* as in Grizzle et al. (2001); Westervelt et al. (2003). For MARLO, six virtual constraints are defined, one for each available actuator.

The output vector y is defined in terms of the configuration variables, q , angular momentum, σ , and a set of parameters κ and β ,

$$y = h(q, \sigma, \kappa, \beta), \quad (37)$$

in such a way that the output has vector relative degree 2 (Isidori 1995, pp. 220) on a subset of interest, $\mathcal{X} \times \mathcal{K} \times \mathcal{B}$. The parameters κ are used to achieve invariance of the *zero dynamics* manifold induced by (37), as shown in Appendix A, while the parameters β will be tuned through optimization to achieve a desirable periodic orbit.

The feedback controller is based on input-output linearization, namely

$$u_{ff}(q, \dot{q}, \kappa, \beta) := -[L_g L_f h(q, \dot{q}, \kappa, \beta)]^{-1} L_f^2 h(q, \dot{q}, \kappa, \beta), \quad (38)$$

$$u_{fb}(q, \dot{q}, \kappa, \beta) := -[L_g L_f h(q, \dot{q}, \kappa, \beta)]^{-1} (K_p y + K_d \dot{y}), \quad (39)$$

with³

$$u = \Gamma(q, \dot{q}, \kappa, \beta) := u_{ff}(q, \dot{q}, \kappa, \beta) + u_{fb}(q, \dot{q}, \kappa, \beta). \quad (40)$$

Along solutions of the closed-loop system,

$$\ddot{y} + K_d \dot{y} + K_p y \equiv 0. \quad (41)$$

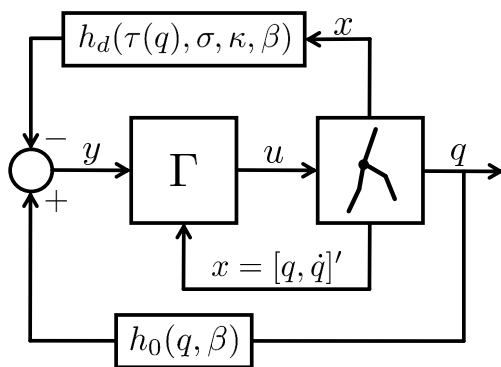


Figure 7. Nonholonomic virtual constraint control schematic.

An explicit choice of $h(q, \sigma, \kappa, \beta)$ is now made,

$$h(q, \sigma, \kappa, \beta) = h_0(q, \beta) - h_d(\tau(q), \sigma, \kappa, \beta), \quad (42)$$

where $h_d(\tau(q), \sigma, \kappa, \beta)$ specifies the desired evolution of the controlled outputs $h_0(q, \beta)$, which are chosen as

$$h_0(q, \beta) = \begin{bmatrix} q_{LA,ST} \\ q_{LA,SW} \\ q_{KA,ST} \\ q_{KA,SW} \\ q_{yT} - \xi(\beta)q_{HA,ST} \\ q_{HA,SW,ABS} \end{bmatrix}, \quad (43)$$

where LA , KA , and HA are abbreviations of leg angle, knee angle, and hip angle respectively, and ST and SW designate the stance and swing legs, as shown in Figure 6. For the lateral controller, a combination of torso roll, q_{yT} , and stance hip, $q_{HA,ST}$, are used.⁴ As in Akbari Hamed et al. (2015), the scalar $\xi(\beta)$ is a free optimization parameter that changes the output configuration. Finally, $q_{HA,SW,ABS}$ represents the absolute swing-hip angle w.r.t. the global vertical axis. The complete output control schematic is shown in Figure 7.

The desired evolution of the controlled outputs is chosen as

$$h_d(\tau(q), \sigma, \kappa, \beta) = h_{d,\tau}(\tau(q), \kappa, \beta) + h_{d,\sigma}(\sigma, \beta), \quad (44)$$

where $h_{d,\tau}(\tau(q), \kappa, \beta)$ and $h_{d,\sigma}(\sigma, \beta)$ specify holonomic and nonholonomic virtual constraints respectively.

The function $h_{d,\tau}(\tau(q), \kappa, \beta) \in \mathbb{R}^6$ is a vector of splines that specifies the desired evolution of defined $h_0(q, \beta) - h_{d,\sigma}(\sigma, \beta)$ in terms of the gait phasing variable $\tau(q)$. Here, the splines are Bézier polynomials, with the i th polynomial given by

$$h_{d,\tau,i}(\tau, \kappa, \beta) := \sum_{k=0}^M \alpha_{i,k} \frac{M!}{k!(M-k)!} \tau^k (1-\tau)^{M-k}, \quad (45)$$

where, as in (Westervelt et al. 2007, pp. 138), the six degree- $(M+1)$ Bézier polynomials are defined by $\alpha(\kappa, \beta) \in \mathbb{R}^{6 \times (M+1)}$, which is derived in Appendix B. The gait phasing variable, $\tau(q)$, is selected to be an affine function of the y position of the center of the hips, $p_{HIP,y}$, and is normalized on the periodic orbit to take values in $[0, 1]$. If $\tau(q) > 1$ outside of the periodic orbit, extended Bézier polynomials defined in Appendix C are used in (45).

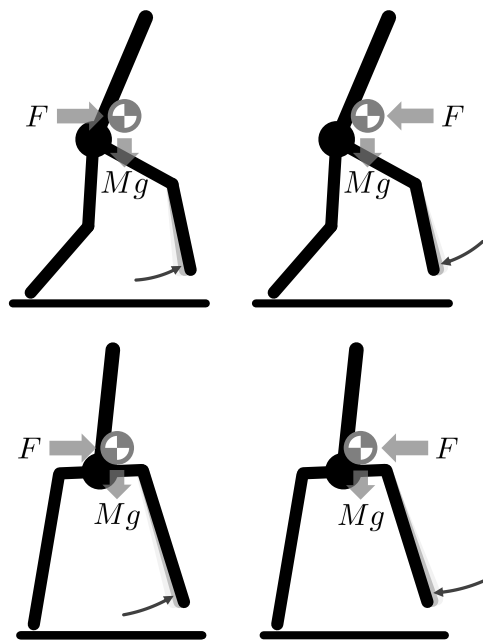


Figure 8. Typical posture changes in response to velocity perturbations from pushes in the sagittal (top) and frontal (bottom) planes. Changes in swing foot placement adapt the gravity moment between the stance foot and the center of mass during the following step.

The nonholonomic virtual constraints are chosen as

$$h_{d,\sigma}(\sigma, \beta) = \begin{bmatrix} 0 \\ k_\sigma(k_1(\beta), \sigma_{yz}) \\ 0 \\ 0 \\ 0 \\ k_\sigma(k_2(\beta), \bar{\sigma}_{xz}) \end{bmatrix}, \quad (46)$$

where σ_{yz} and $\bar{\sigma}_{xz}$ are angular momentum in the sagittal and frontal planes and the nonholonomic function is defined as

$$k_\sigma(k_i, \sigma_j) := k_{i,1}\sigma_j + k_{i,2}\sigma_j^2 + k_{i,3}\sigma_j^3, \quad (47)$$

where $k_i \in \mathbb{R}^3$ is a set of scalars for the cubic polynomial. The complete output equation using (37) and (42)-(46) is

$$y = \begin{bmatrix} q_{LA,ST} \\ q_{LA,SW} \\ q_{KA,ST} \\ q_{KA,SW} \\ q_{yT} - \xi q_{HA,ST} \\ q_{HA,SW,ABS} \end{bmatrix} - \begin{bmatrix} 0 \\ k_\sigma(k_1, \sigma_{yz}) \\ 0 \\ 0 \\ 0 \\ k_\sigma(k_2, \bar{\sigma}_{xz}) \end{bmatrix} - h_{d,\tau}(\tau). \quad (48)$$

The inclusion of angular momentum in the second and sixth components of $h_{d,\sigma}$ allows step length and width to vary with velocity. In the optimization phase, values for $k_1(\beta)$ and $k_2(\beta)$ will be chosen such that a perturbation in velocity, and attendant deviation of σ , results in a corrective change in swing foot placement, as shown in Figure 8. With respect to the sagittal plane, these changes adjust the amount of time the center of mass spends behind, versus in front of the stance foot. With respect to frontal plane, these changes adjust the magnitude of the lateral gravity moment proportional to the width between the stance foot and the center of mass. Adding these corrective changes after velocity perturbations results

in quicker convergence to the periodic orbit. Additionally, lateral stabilization through step width adjustments is shown to be more efficient than direct actuation in Kuo (1999). For more details, see Kajita et al. (1992); Pratt and Tedrake (2006); Koolen et al. (2012); (Griffin 2016b, pp. 148).

Remarks on $h_{d,\sigma}$: In practice, we have included additional responses to velocity perturbations (e.g., changing stance and swing knee angles to regulate lateral velocity through modified ground reaction forces and step duration). To make the introduction of nonholonomic virtual constraints straightforward, the current choice of $h_{d,\sigma}$ is limited to swing foot placement. A thorough comparison of nonholonomic virtual constraints and LIP-based swing foot placement is provided in Griffin and Grizzle (2015a).

Remarks on $\bar{\sigma}_{xz}$: During a nominal step, the robot rotates laterally both toward and away from the stance foot; hence, σ_{xz} is negative and positive within the same step. In practice, we found it beneficial to use only the portion of σ_{xz} associated with rolling away from the stance leg during the later part of each step. To keep control inputs (40) continuous and smooth, we define $\bar{\sigma}_{xz}$ as

$$\bar{\sigma}_{xz} := \begin{cases} 0 & \text{if } \sigma_{xz} < 0 \\ \sigma_{xz} e^{(\frac{-30}{\sigma_{xz}^2})} & \text{if } \sigma_{xz} \geq 0 \end{cases}, \quad (49)$$

which uses $e^{(\frac{-30}{\sigma_{xz}^2})}$ to smoothly transition to non-zero values of σ_{xz} . See Figure 28 in Appendix D for a visual comparison of σ_{xz} and $\bar{\sigma}_{xz}$.

5.3 Robust Control Optimization Configuration and Control Solutions

The cost function for the nominal periodic orbit is based on energetic efficiency and is defined as

$$\mathcal{J}_0 := \frac{1}{\text{step length}} \int_0^{T_0} \sum_{i=1}^6 |u_i \dot{q}_{m,i}| dt, \quad (50)$$

where step length is the distance between the stance and swing feet at impact,⁵ T_0 is the period, u is the 6-vector of motor torques, and \dot{q}_m is the corresponding 6-vector of motor angular velocities, which is obtained from the link velocities and gear ratios as in Ramezani et al. (2014). The product of u_i and $\dot{q}_{m,i}$ is the instantaneous mechanical power from each motor.

The nominal periodic orbit was computed for walking on level ground (i.e., $d_0 = 0$) by optimizing (25), with nominal cost (50), subject to the hybrid dynamic model (65) given in Appendix A and the following constraints: leg and hip motor torques saturate at 4 Nm and 2 Nm respectively, minimum vertical ground reaction forces of 250 N and maximum required friction coefficient of 0.5, minimum knee bend of 20° to avoid hyperextension, maximum combined hip angles of 190° to avoid leg collision, maximum link velocities of 200 deg/s for (q_1, q_2) and 60 deg/s for q_3 , average walking speed between 0.5-1 m/s, minimum swing foot clearance of 0.1 m over stance foot, and backward swing-foot velocity at impact. Constraints based on ground reaction forces and physical limitations of MARLO also apply to perturbed steps.

The weight matrix Q in (22) is selected such that torso roll and pitch squared errors are multiplied by 4, hip squared

errors are multiplied by 2, and velocity squared errors are divided by four. The weight matrix R in (23) is selected such that it has one fifth the base weighting of Q . The variables N_s and w_{ij} from (25) are selected such that costs are generated for two steps following a disturbance (i.e., $N_s = 2$), and the second perturbed step is multiplied by 3 (i.e., $w_{i2} = 3$). The rationale for this is to enable the optimizer to choose actions that may deviate more from the nominal trajectory directly following a disturbance, but result in quicker convergence to nominal conditions in subsequent steps.

The control solutions are found offline with fmincon in MATLAB, using the nonholonomic-virtual-constraints (NHVC) given in Section 5.2. For comparison purposes, a nominal control solution, NHVC₀, is defined for terrain-height disturbances $D = \{\pm 2 \text{ cm}, \pm 4 \text{ cm}\}$ and center of mass velocity disturbances in the x and y directions $V_x = \{\pm 7.5 \text{ cm/s}, \pm 15 \text{ cm/s}\}$ and $V_y = \{\pm 15 \text{ cm/s}, \pm 30 \text{ cm/s}\}$ for a total of twelve disturbances.

To test the efficacy of new concepts and establish best practices for selecting optimization disturbances, additional control solutions are found using different optimization configurations. Configurations consist of the choice of nonholonomic function and optimization disturbance profile. The control solutions are optimized using the parameter values of NHVC₀ as initial values and using the disturbance profiles indicated in Table 1. First, to investigate the utility of using nonholonomic outputs, a holonomic control solution, HVC, is optimized with $k_1, k_2 = 0$ in (46), using the same disturbance profile as NHVC₀. In order to find a stable solution for HVC, it is necessary to include optimization costs associated with the highest eigenvalue of the linearized Poincaré map, as done in Chevallereau et al. (2009). Additionally, different nonholonomic functions are tested by using a linear (Deg.1) or quadratic (Deg.2) polynomial in place of (47). Finally, the remaining control solutions evaluate the effect of different disturbance configurations, such as incorporating a decreased (–) or increased (+) range of disturbances or only terrain (D) or velocity (V) disturbances. In the next section, these control solutions are evaluated in simulation. Additional control solutions for experiments are introduced in Section 7.1. Source code for control design and simulation is available at Griffin (2016a).

6 Simulation Results

Control solutions are compared in simulation to evaluate concepts introduced in this paper and to test the relative benefit of various disturbances for the robust control optimization. The gait designs of Table 1 are simulated under the influence of external forces and over terrain with varying height. Section 6.1 provides an evaluation of periodic flat-ground walking behavior and Section 6.2 provides an evaluation of walking with disturbances. Section 6.2.1 evaluates the performance under persistent, repeated disturbances, which is a means to assess “steady-state” behavior under disturbances, whereas Section 6.2.2 focuses on transient aspects by giving results for recovery after a single disturbance. Discussion and interpretation of the simulation results are given in Section 6.3. A video illustrating the results is available at Dynamic Legged Locomotion Lab (2016).

Table 1. Periodic-walking behavior of control solutions that result from different optimization configurations. $\sum w_{ij} \mathcal{J}_{ij} / \mathcal{J}_0$ is the ratio of disturbance- to efficiency-based optimization costs in (25). MCOT, Forward Walking Speed, and Maximum Eigenvalue of Linearized Poincaré Map are detailed in Section 6.1.

Control	Optimization Disturbance Profile			$\sum w_{ij} \mathcal{J}_{ij} / \mathcal{J}_0$ in (25)	MCOT (51)	Impact Losses (J)	Forward Walking Speed (m/s)	Maximum Eigenvalue of Linearized Poincaré Map	$\xi(\beta)$ (43)
	D (cm)	V_x (cm/s)	V_y (cm/s)						
Nominal Control Solution									
NHVC ₀	$\pm 2, \pm 4$	$\pm 7.5, \pm 15$	$\pm 15, \pm 30$	2.1	0.240	6.7	0.736	0.61	0.276
Varied Nonholonomic Function (47)									
HVC	$\pm 2, \pm 4$	$\pm 7.5, \pm 15$	$\pm 15, \pm 30$	7.9	0.231	7.5	0.780	0.92	0.284
NHVC _{Deg.1}	$\pm 2, \pm 4$	$\pm 7.5, \pm 15$	$\pm 15, \pm 30$	2.8	0.239	7.5	0.770	0.74	0.299
NHVC _{Deg.2}	$\pm 2, \pm 4$	$\pm 7.5, \pm 15$	$\pm 15, \pm 30$	1.8	0.239	7.1	0.729	0.69	0.239
Decreased (-) or Increased (+) Terrain and Velocity Disturbances (DV)									
NHVC _{DV-}	$\pm 1, \pm 2$	$\pm 3.75, \pm 7.5$	$\pm 7.5, \pm 15$	1.0	0.242	7.0	0.764	0.69	0.246
NHVC _{DV+}	$\pm 4, \pm 8$	$\pm 15, \pm 30$	$\pm 25, \pm 50$	7.2	0.254	7.3	0.778	0.70	0.341
Terrain Disturbances Only (D)									
NHVC _{D-}	$\pm 1, \pm 2$	\emptyset	\emptyset	0.5	0.241	6.9	0.765	0.72	0.287
NHVC _D	$\pm 2, \pm 4$	\emptyset	\emptyset	0.7	0.237	7.1	0.744	0.67	0.266
NHVC _{D+}	$\pm 4, \pm 8$	\emptyset	\emptyset	1.1	0.246	7.0	0.769	0.79	0.345
Velocity Disturbances Only (V)									
NHVC _{V-}	\emptyset	$\pm 3.75, \pm 7.5$	$\pm 7.5, \pm 15$	0.4	0.237	6.9	0.749	0.72	0.314
NHVC _V	\emptyset	$\pm 7.5, \pm 15$	$\pm 15, \pm 30$	1.3	0.235	7.2	0.741	0.75	0.291
NHVC _{V+}	\emptyset	$\pm 15, \pm 30$	$\pm 25, \pm 50$	4.9	0.248	7.2	0.788	0.70	0.291

6.1 Walking on Flat Ground without External Disturbances

Each of the controllers in Table 1 is initially simulated over flat ground with no external perturbations. To evaluate the energetic efficiency of a control solution, the mechanical cost of transport (MCOT) is calculated as

$$\text{MCOT} := \frac{1}{Mgd_y} \int_0^{T_0} \sum_{i=1}^6 \max(u_i \dot{q}_{m,i}, 0) dt, \quad (51)$$

where M is the total mass of the biped, g is the acceleration due to gravity, d_y is the forward travel distance, and only the positive work of each actuator is considered. While \mathcal{J}_0 (50) is suitable for generating a robot-specific efficiency cost during optimization, the dimensionless MCOT normalizes efficiency by a robot's weight, which enables a fair efficiency comparison between different robot platforms. The reader is referred to Table 8 in Appendix E and Collins et al. (2005) for a review of MCOT for various legged robots.

The forward walking speed is calculated for each step using the forward change in the center of mass position and step time. The lateral velocity is calculated for each step using the lateral change in the center of mass position and step time. The lateral velocity direction generally alternates with the left and right stance phases.

To evaluate the stability of a control solution's fixed point (i.e., periodic orbit), the eigenvalues of the linearized Poincaré map are computed, with the maximum magnitude of the eigenvalues given in Table 1. For the current control implementation, yaw is not regulated. Consequently, the eigenvalue associated with yaw is 1, as proved in (Shih et al. 2012, Propositions 3 and 4), and is not included in the comparison.



Figure 9. Sagittal view of NHVC₀ control solution walking downhill with repeated -10 cm changes in terrain height.

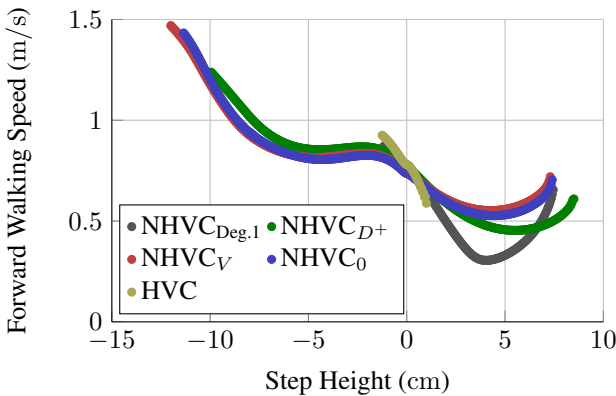
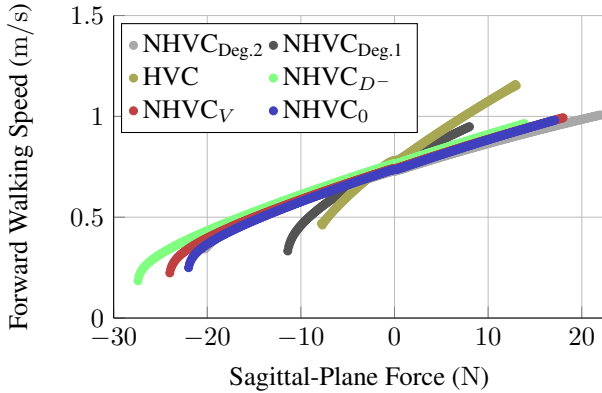
6.2 Walking with Disturbances

Terrain and push disturbances are used to evaluate each control solution. For terrain disturbances, changes in terrain height consist of a vertical displacement of d (cm) per step. Figure 3 shows an example of a single vertical displacement, d_i , and Figure 9 shows walking with repeated -10 cm displacements in simulation. For push disturbances, horizontal forces of F (N) are applied to the center of mass over the duration of an entire step. This induces a velocity perturbation to the robot without the complication of terrain variation. Assuming left-right symmetry of a robot, push direction (forward or backward) in the sagittal plane determines the control response. In the frontal plane, however, whether a push is away from or toward the stance leg affects the appropriate control response, as illustrated in Figure 8.

Remark: During optimization, velocity disturbances are applied as step changes to the center of mass velocity in (14). For evaluation in Section 6.2, velocity perturbations are induced by applying external forces to the center of

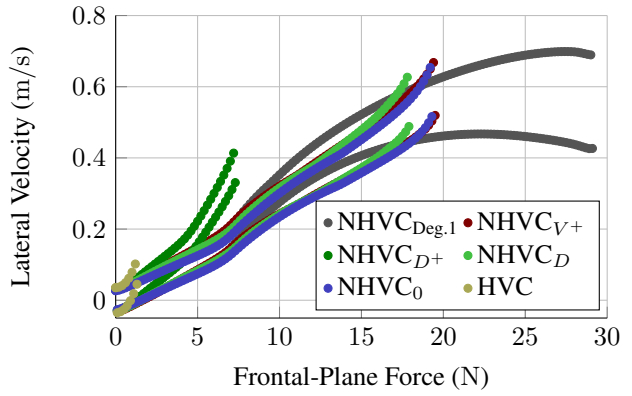
Table 2. Disturbance limits of control solutions. Bold text indicates best and worst result for each column.

Control	Step Disturbance (cm)			Sagittal-Plane Force (N)			Frontal-Plane Force (N)		
	Min.	Max.	Range	Min.	Max.	Range	Min.	Max.	Range
NHVC ₀	-11.35	7.40	18.75	-22.2	17.1	39.3	-20.2	20.2	40.4
HVC	-1.25	1.35	2.60	-8.4	13.0	21.4	-2.4	2.4	4.8
NHVC _{Deg.1}	-1.15	7.45	8.60	-11.6	8.0	19.6	-29.5	29.5	59.0
NHVC _{Deg.2}	-11.70	7.20	18.90	-21.1	22.0	43.1	-19.7	19.6	39.3
NHVC _{DV-}	-7.00	7.25	14.25	-22.3	12.6	34.9	-16.1	16.1	32.2
NHVC _{DV+}	-10.75	7.60	18.35	-21.8	17.4	39.2	-18.5	18.5	37.0
NHVC _{D-}	-6.10	7.25	13.35	-27.5	13.9	41.4	-12.8	12.8	25.6
NHVC _D	-10.90	7.35	18.25	-20.2	15.4	35.6	-18.8	18.8	37.6
NHVC _{D+}	-9.95	8.50	18.45	-22.6	13.4	36.0	-8.5	8.5	17.0
NHVC _{V-}	-10.65	7.45	18.10	-21.5	16.2	37.7	-15.8	15.8	31.6
NHVC _V	-12.00	7.30	19.30	-24.2	18.0	42.2	-18.5	18.5	37.0
NHVC _{V+}	-10.10	6.80	16.90	-22.4	18.4	40.8	-20.4	20.4	40.8

**Figure 10.** Walking speed vs. sustained terrain disturbances.**Figure 11.** Walking speed vs. sustained sagittal-plane force.

mass over an entire step, which maintains continuous single support dynamics.

6.2.1 Repeated Disturbance Limits Here, control solutions are compared under the action of a persistent disturbance whose magnitude is gradually increased each step until the robot falls. A fall occurs when requiring a friction coefficient greater than 0.6 or losing momentum and tumbling sideways or backward. For disturbance limits with changes in terrain height, each control solution is initialized on the periodic orbit, and then terrain height increases each step as $d_{k+1} = d_k + 0.5$ mm, where k is the step number. Once a

**Figure 12.** Lateral velocity vs. sustained frontal-plane force. The lateral velocity alternates with each stance leg because forces are applied in one direction. Hence, there are separate curves for the left and right stance phases of each control solution.

fall occurs, the simulation is reset from the periodic orbit, and a decrease of 0.5 mm is applied to d_k until failure. The same procedure is applied through sagittal and frontal plane forces with 0.1 N increments. The results of repeated disturbance simulations for all control solutions are summarized in Tables 2 and 3, and, for sets of control solutions that exhibit the range of observed behaviors, the perturbed velocities for each step are plotted in Figures 10–12. Because the robot model is symmetric, frontal-plane forces only need to be evaluated in one direction.

6.2.2 Transient Response to Perturbations Additional simulations are performed to evaluate the transient response of each control solution to individual terrain and push disturbances. The HVC control solution is unable to recover from the disturbances used here, as shown in Figure 13, and is not included in the remaining analysis. Velocity deviations after terrain disturbances of ± 2 cm, ± 4 cm, and ± 8 cm are shown in Figure 14.

For push disturbances, 50 N forces are applied over the length of an entire step in either the sagittal or frontal planes. Sagittal-plane pushes are applied in the forward and backward directions, as shown in Figure 15. For 3D walking, the sagittal and frontal plane dynamics are coupled,

Table 3. Disturbance-limit averages of control solutions, which are grouped by optimization configuration. Bold text indicates greatest range for each category. HVC, NHVC_{Deg,1}, and NHVC_{Deg,2} are not included in the group averages.

Optimization Configuration Group	Step Disturbance (cm)			Sagittal-Plane Force (N)			Frontal-Plane Force (N)		
	Min.	Max.	Range	Min.	Max.	Range	Min.	Max.	Range
Disturbance Type									
Terrain and Velocity Disturbances	-9.7	7.4	17.1	-22.1	15.7	37.8	-18.3	18.3	36.5
Terrain Disturbances Only (<i>D</i>)	-9.0	7.7	16.7	-23.4	14.2	37.7	-13.4	13.4	26.7
Velocity Disturbances Only (<i>V</i>)	-10.9	7.2	18.1	-22.7	17.5	40.2	-18.2	18.2	36.5
Disturbance Magnitude									
Moderate Disturbances	-11.4	7.4	18.8	-22.2	16.8	39.0	-19.2	19.2	38.3
Decreased Disturbances (-)	-7.9	7.3	15.2	-23.8	14.2	38.0	-14.9	14.9	29.8
Increased Disturbances (+)	-10.3	7.6	17.9	-22.3	16.4	38.7	-15.8	15.8	31.6

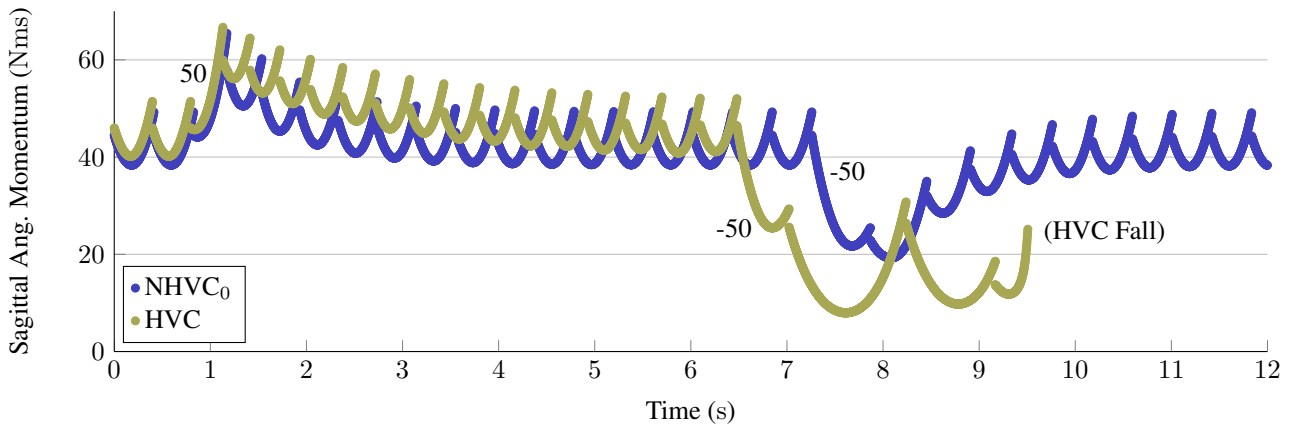


Figure 13. Sagittal-plane angular momentum stabilization after pushes in sagittal plane. Forward and backward 50 N pushes occur over the entire third and nineteenth steps respectively. Whereas the nonholonomic control solution (NHVC₀) is able to recover from the disturbances, the holonomic control solution (HVC) does not return to its nominal periodic orbit following the forward push then slows down and falls laterally after the backward push. During each step, angular momentum decreases when the center of mass is behind the stance foot then increases once the center of mass is in front of the stance foot. Step decreases in angular momentum occur at step transition due to impact losses. Step times vary between the two control solutions.

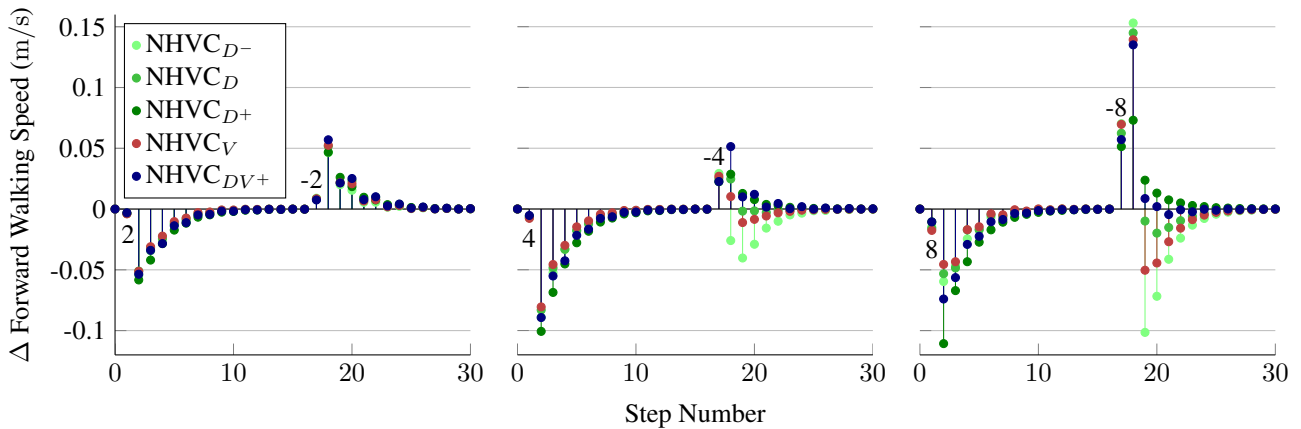


Figure 14. Sagittal-plane velocity deviations after ± 2 cm (left), ± 4 cm (center), and ± 8 cm (right) terrain disturbances. Step-up and step-down disturbances occur on the first and seventeenth steps respectively. When converging back to the periodic orbit, sagittal-plane velocity is not necessarily monotonic due to the coupled dynamics of the sagittal and frontal planes. Following step-up disturbances outside of the ± 2 cm range used for optimization, NHVC_{D-} is more destabilized than the other control solutions.

as demonstrated by the simultaneous frontal-plane velocity deviations occurring with sagittal-plane pushes shown in Figure 16. Lateral perturbations caused by changes in forward walking speed are just one example of coupled dynamics. A loss in forward walking speed results in more time spent on a single stance leg, which subsequently causes

a longer lateral gravity moment and increased lateral velocity by the end of the step. Likewise, a gain in forward walking speed results in less time spent on a single stance leg and a decreased lateral velocity. These coupled behaviors are evident in Figures 15 and 16. The role of synchronization

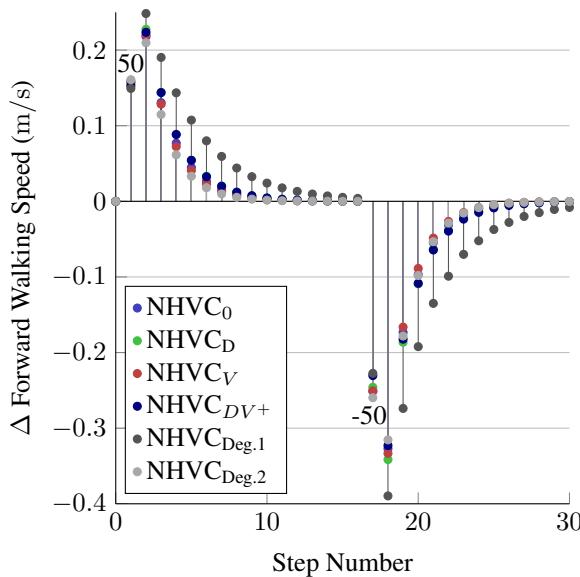


Figure 15. Sagittal-plane velocity deviations after pushes in sagittal plane. Forward and backward 50 N pushes occur over the entire first and seventeenth steps respectively. Figure 16 shows the simultaneous frontal-plane velocity deviations.

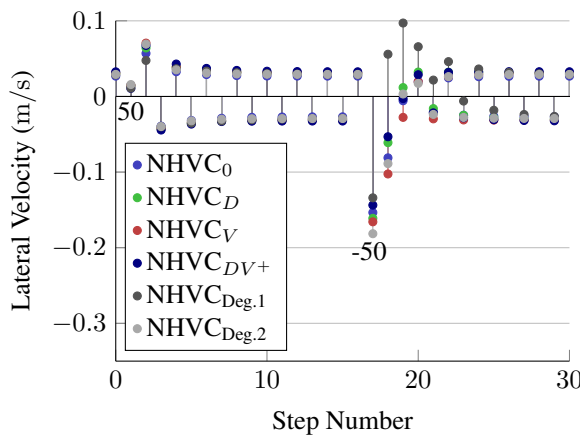


Figure 16. Frontal-plane velocity deviations after pushes in sagittal plane.

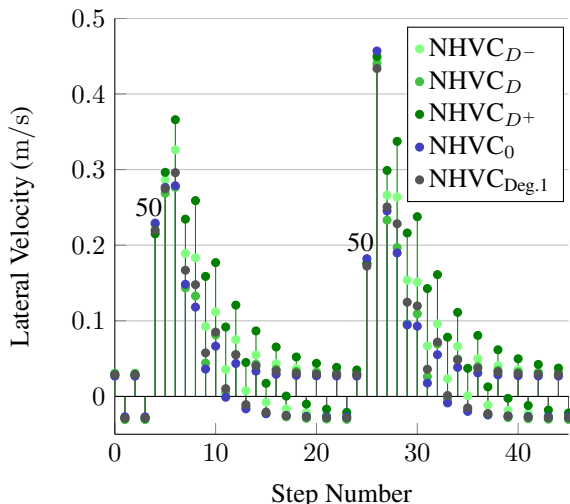


Figure 17. Frontal-plane velocity deviations after pushes in frontal plane. Lateral 50 N pushes away from and toward the stance leg occur over the entire fourth and twenty-fifth steps respectively.

Table 4. Single-step pushes and corresponding impulses for NHVC_0 .

Push Disturbance	Force (N)		Step Time (s)	Impulse (Ns)	
	x	y		x	y
None, Periodic Orbit	0	0	0.412	0	0
Forward	0	50	0.347	0	17.4
Backward	0	-50	0.609	0	-30.4
Away from Stance	50	0	0.410	20.5	0
Toward Stance	50	0	0.422	21.1	0

of pendular motion in the sagittal and frontal planes to gait stability is studied in Razavi et al. (2015).

Frontal-plane pushes are applied in a single direction, as shown in Figure 17, but are timed such that the first lateral push is away from the stance leg and the second push is toward the stance leg. Both lateral-push behaviors are depicted in Figure 8 (bottom) for clarification.

Impulses corresponding to single-step pushes for the NHVC_0 control solution are provided in Table 4. A backward push results in the longest step time and greatest corresponding impulse.

6.3 Discussion of Simulation Results

Each of the control solutions in Table 1 have similar nominal periodic orbits with respect to forward walking speed, step length, and foot clearance at mid-step; nevertheless, as documented above, their responses to disturbances vary greatly. Sections 6.3.1-6.3.3 examine these performance differences and discuss the benefits of different optimization configurations. Section 6.3.4 introduces an evaluation of walking efficiency over a variety of terrain conditions. Finally, Section 6.3.5 closes with a brief general discussion.

6.3.1 Choice of Holonomic and Nonholonomic Outputs
The control solutions using nonholonomic outputs (NHVC) outperform the holonomic control solution (HVC). First, HVC is the only control solution that cannot recover from the disturbances used in Section 6.2.2. Second, as shown in Table 2, HVC has the smallest range of admissible repeated disturbances. HVC can handle greater forward forces than $\text{NHVC}_{\text{Deg.1}}$, but it performs the worst for all other tested disturbances. Third, HVC exhibits the greatest deviations in velocity within its operating range, as shown in Figures 10-12. Finally, as shown in Table 1, the NHVC solutions have a smaller spectral radius (i.e., maximum magnitude of the Poincaré map eigenvalues) than HVC, suggesting quicker convergence to the periodic orbit after a (small) disturbance. Compared with HVC in Figure 13, NHVC_0 demonstrates this quicker convergence and improved disturbance attenuation. The improved performance of the NHVC solutions is attributed to their added ability to regulate walking posture with velocity (e.g., adjusting sagittal step distance with forward walking speed, as shown in Figure 18).

Many of the NHVC solutions have a similar recovery from velocity perturbations, as shown in Figures 15 and 16. This is, in part, due to using local optimization with repeated initial values. Consistent solutions for $k_1(\beta)$ and $k_2(\beta)$ in the nonholonomic function, (46),

determine how posture adapts with velocity. There is more variability when changing the underlying nonholonomic function (i.e., HVC, NHVC_{Deg.1}, and NHVC_{Deg.2}) than when changing optimization disturbances, as shown in Figure 18. Implementing nonholonomic functions other than simple polynomials would likely enable additional variability.

6.3.2 Choice of Optimization Disturbance Type A A comparison of NHVC solutions reveals that there are clear benefits to including velocity disturbances in the robust control optimization. First, NHVC_V, which incorporates only velocity disturbances during optimization, handles a wider range of repeated terrain disturbances than the other NHVC solutions (see Table 2). In contrast, NHVC_{D+} and NHVC_{D-}, which incorporate only terrain disturbances during optimization, handle the smallest ranges of frontal-plane forces and have the slowest recoveries following lateral pushes (see Figure 17). Finally, with respect to repeated disturbances, solutions incorporating only terrain disturbances perform worse than solutions incorporating velocity disturbances (see Table 3). This difference in performance likely occurs because applying individual terrain disturbances during the robust control optimization does not perturb velocity to the same extent as repeated terrain disturbances. We propose that by including velocity disturbances in the robust control optimization, nonholonomic outputs are obliged to make constructive posture adjustments over a wider range of walking speeds, including speed changes that occur when walking uphill or downhill. Our analysis has considered only two types of disturbances. Investigating additional classes of disturbances to be included in the control design process should be a worthwhile endeavor.

6.3.3 Choice of Optimization Disturbance Magnitude The size of disturbances used for the robust control optimization is also significant. NHVC_{D-}, which incorporates smaller disturbances during optimization than NHVC_D or NHVC_{D+}, exhibits greater deviations in velocity following the terrain disturbances illustrated in Figure 14. As the size of terrain disturbances incorporated during optimization increases, control solutions handle steeper uphill terrain (see Table 2) and require a lower friction coefficient for the majority of the repeated terrain disturbances illustrated in Figure 19. Incorporating larger disturbances for the robust control optimization does not, however, indiscriminately improve performance. As shown in Table 3, solutions incorporating only moderate disturbances handle the widest range of repeated terrain and force disturbances. For the current control implementation, we propose that incorporating larger disturbances during optimization results in the adherence to performance criteria (e.g., required friction coefficient) for a broader range of disturbances; however, this generalization comes at a cost in other aspects (e.g., handling a more limited range of repeated disturbances). This tradeoff could be avoided with a control implementation that enables tailoring for specific conditions (e.g., switching among a library of control solutions).

6.3.4 Walking Efficiency for Various Terrain Conditions Walking efficiency should be evaluated for a variety of terrain conditions and, as emphasized by Saglam and Byl (2014a), within the context of robustness. Each of the control

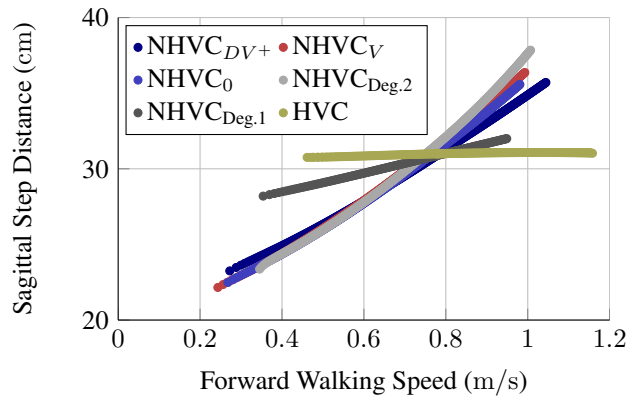


Figure 18. Sagittal step distance vs. forward walking speed. Details on how sagittal step distance regulates sagittal velocity are available in Griffin and Grizzle (2015a).

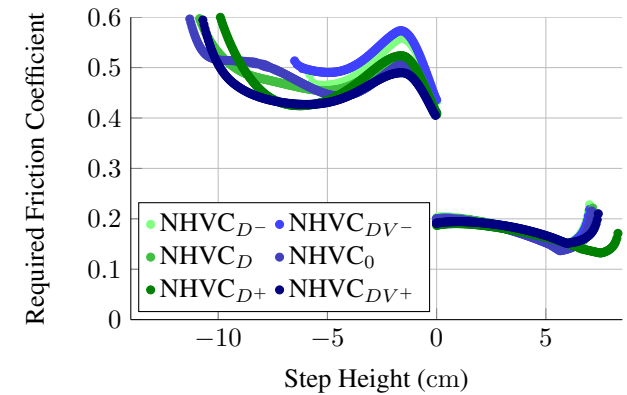


Figure 19. Required friction coefficient vs. sustained terrain disturbances. During downhill walking, the extended controller defined in Appendix C requires a greater friction coefficient. Essentially, the stance knee quickly bends to lower the biped.

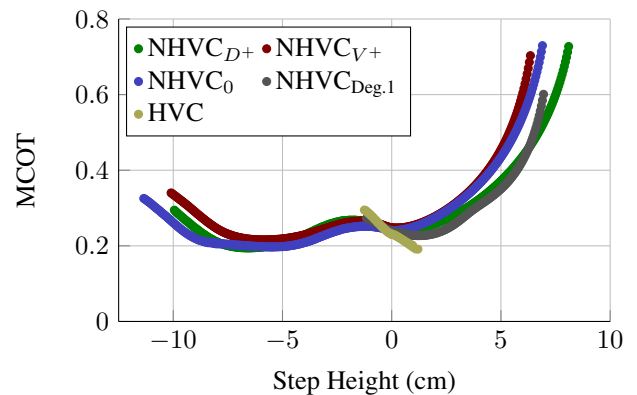


Figure 20. MCOT vs. sustained terrain disturbances.

solutions in Table 1 exhibits a similar periodic MCOT. HVC has the lowest periodic MCOT, but when considering the limited range of traversable terrain for this control solution (see Table 2), the *flat-ground* walking efficiency is less relevant. Additionally, just as Martin et al. (2014b); Xi et al. (2015) consider gait efficiency for a range of velocities, for practical walking applications, we propose that efficiency should be evaluated for a variety of terrain conditions. MCOT is plotted for a range of repeated terrain disturbances in Figure 20. For the NHVC solutions, MCOT increases

Table 5. Simulation-based periodic-walking behavior of control solutions used on the robot.

Control	Optimization Disturbance Profile			Ratio of $\sum w_{ij} \mathcal{J}_{ij}$ / \mathcal{J}_0 in (25)	MCOT (51)	Impact Losses (J)	Forward Walking Speed (m/s)	Maximum Eigenvalue of Linearized Poincaré Map	$\xi(\beta)$ (43)
	D (cm)	V_x (cm/s)	V_y (cm/s)						
Optimized Prior to Robot Experiments									
NHVC ₀	$\pm 2, \pm 4$	$\pm 7.5, \pm 15$	$\pm 15, \pm 30$	2.1	0.240	6.7	0.736	0.61	0.276
NHVC ₀ ^{Poincaré}	$\pm 2, \pm 4$	$\pm 7.5, \pm 15$	$\pm 15, \pm 30$	1.8	0.234	7.3	0.732	0.58	0.273
NHVC ₁	$\pm 3, \pm 6$	$\pm 15, \pm 30$	$\pm 20, \pm 40$	4.7	0.219	8.0	0.751	0.75	0.258
NHVC ₂	$\pm 3, \pm 6$	± 20	± 30	2.4	0.217	7.5	0.732	0.66	0.232
Optimized After Initiating Robot Experiments									
NHVC ₃	$\pm 3, \pm 6$	± 30	± 30	3.0	0.267	7.3	0.811	0.74	0.246

with uphill terrain because of the additional work required to raise the center of mass. For downhill terrain, MCOT decreases with moderate declines, but increases with more severe declines. This eventual increase arises from the larger impact losses associated with downhill walking. The effects of impact losses on MCOT are well illustrated by HVC, because it makes no velocity-dependent posture adjustments. Uphill walking decreases HVC's impact losses and MCOT, whereas downhill walking increases HVC's impact losses and MCOT.

6.3.5 General Discussion The control solutions using nonholonomic outputs are able to handle a wide range of disturbances and terrain conditions. NHVC₀ recovers from backward impulses of -30.4 Ns, handles about a 40 N range of sustained forces in the sagittal and frontal planes, and handles an 18.8 cm range of repeated terrain disturbances. Such robustness is desirable because it allows the robot to handle disturbances and difficulties associated with the robot hardware.

7 Experimental Results

Experiments are conducted on MARLO both indoors and outdoors. Section 7.1 introduces the control solutions implemented on the robot. Section 7.2 describes the setup for the experiments. Section 7.3 presents the results of the experiments, with discussion given in Section 7.4. Videos of indoor and outdoor experiments are available at Dynamic Legged Locomotion Lab (2016).

7.1 Control Solutions

The control solutions used on the robot are designed for outdoor terrain. Optimization terrain disturbances (D) are based on outdoor measurements and previous planar experiments with uneven terrain in Griffin and Grizzle (2015b). Optimization velocity disturbances (V) are based on forward walking speed and velocity changes attendant with repeated terrain disturbances. The nominal control solution based on nonholonomic virtual constraints, NHVC₀, is carried forward to the experiments. Prior to beginning the experimental phase of the work, additional controller designs similar to NHVC₀ are performed, as indicated in Table 5. The NHVC₀^{Poincaré} control solution has the same disturbance profile as NHVC₀ with an additional penalty included on the spectral radius of the linearized Poincaré map (i.e., on the peak magnitude of the eigenvalues).

One additional control solution is optimized after initiating the experiments. After the first day of outdoor walking, laterally-sloped terrain is identified as a significant perturbation to the gait of the robot. To account for this, an additional controller, NHVC₃, is designed with equal emphasis on velocity disturbances in the frontal and sagittal planes.

Remark: Holonomic control solutions are not implemented on the robot for a few reasons. First, the holonomic control solution HVC is thoroughly evaluated against nonholonomic control solutions in Section 6 and exhibits the worst performance. Second, we have tested holonomic control solutions on MARLO in Buss et al. (2014, 2016), and they were only able to handle relatively flat ground in 3D. Furthermore, these holonomic controllers required an event-based, hand-tuned method of initialization, which is not well-suited for the current experimental setup.

7.2 Experimental Setup

Virtual constraints resulting from the optimization process are implemented on the robot without modification. The feedback controller (40) is simplified as follows. In place of u_{ff} , constant 0.5 Nm torques are added to the stance leg and hips to provide some friction and gravity compensation. In place of the decoupling matrix $L_g L_f h(q, \dot{q}, \kappa, \beta)$, a constant matrix is used to relate y to u_{fb} . Constant decoupling matrices are also used in Buss et al. (2014, 2016). Additionally, commanded motor torque, u , is bounded at 5 Nm for the legs and 3 Nm for the hips. These bounds are greater than those used in optimization to compensate for unmodeled friction and other drivetrain inefficiencies on the actual robot.

Impact is detected by a rapid deflection in the springs when the swing foot contacts the ground. After swapping stance legs, α_0 from Appendix B updates such that $y = 0$. On the robot, there are no instantaneous jumps in the post-impact velocities, so, in place of updating α_1 such that $\dot{y} = 0$, α_1 updates to maintain its nominal difference with respect to α_0 on the periodic orbit. After control updates, torque bounds are initialized at 0 Nm and linearly scaled back to nominal values while $0 < \tau < 0.1$, which limits any counterproductive control inputs during the brief period of double support.

Joint angular velocities are estimated from encoder readings through numerical differentiation. It is a standard problem that such estimates appear "quite noisy" in comparison to the clean signals available in simulation. On

MARLO, a low-pass Butterworth filter based on Butterworth (1930) attenuates only high-frequency “noise”, because the cutoff frequency is necessarily high to limit phase delay in the feedback controller. Angular velocity estimates are particularly “noisy” following impacts and on the hip joint angles, which are measured on the motor side of a belt transmission. Consequently, the derivative term of the controller at the hip-angle only considers the h_0 component of (42) when calculating \dot{y} .

The gait phasing variable, τ , determines the progression of control trajectories, and angular momentum, σ , determines the velocity-based changes of control trajectories. Both τ and σ are critical for implementing nonholonomic virtual constraints. First-order filters for their estimation from measured quantities are specifically designed. Section 7.2.1 defines the phase estimator for τ , and Section 7.2.2 defines a reduced-order Luenberger observer for σ . Comparisons of original signals and their estimated counterparts are provided in Appendix D.

Finally, in the walking experiments, the robot is initialized from a standing position. The use of nonholonomic virtual constraints makes initialization straightforward, because the controller automatically adjusts step length with forward velocity. Under the evaluated controllers, initializing the robot from a static pose and hand-guiding it forward through a few steps is sufficient to enter the basin of attraction. The initialization process is illustrated in Dynamic Legged Locomotion Lab (2016).

7.2.1 Phase Estimator An estimator is used in place of direct measurement of the gait phasing variable. This is done because when $\dot{\tau}$ is determined through numerical differentiation, it presents unacceptable oscillations after impacts, which transfer to the torque signals determined by the controller.

The phase estimator is defined as

$$\dot{\hat{\tau}} := \frac{1}{T} + L(\hat{\tau})(\tau - \hat{\tau}), \quad (52)$$

where $\hat{\tau}$ is the estimated gait phasing variable, T is the duration of the previous step, and $L(\hat{\tau})$ is the observer gain. The term $\frac{1}{T}$ is interpreted as a model for the evolution of the normalized phase variable τ , and $L(\hat{\tau})(\tau - \hat{\tau})$ is the correction term based on observation of τ . Hence, $L(\hat{\tau})$ determines the relative dependence of the estimated phase on the time-based model and the measured gait-phasing variable. Because the numerical estimates of joint velocities appear to be most inaccurate immediately following an impact, $L(\hat{\tau})$ is chosen such that (52) emphasizes the time-based model immediately following impact and then smoothly returns to accurately tracking τ by the end of the step. Specifically, $L(\hat{\tau})$ is defined as

$$L(\hat{\tau}) := \begin{cases} 20\hat{\tau} & \text{if } \hat{\tau} < 1 \\ 20 & \text{if } \hat{\tau} \geq 1 \end{cases}. \quad (53)$$

Remarks: (a) During the first step of an experiment, previous step duration, T , is undefined. Therefore, (52) is modified such that $\frac{1}{T} = 0$ and $L(\hat{\tau}) = 20$. (b) In simulation, the estimated phase variable, $\hat{\tau}$, tracks well with τ and provides a reliable estimate of $\dot{\tau}$, as shown in Figure 27 in Appendix D. (c) $\frac{1}{T}$ is a suitable model for the evolution of

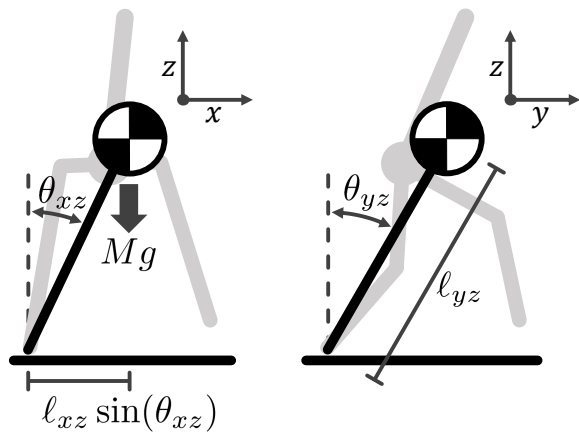


Figure 21. Simplified model for the reduced-order Luenberger observer. Two separate observers estimate σ for the frontal (left) and sagittal (right) planes.

the gait phasing variable $\tau(q)$ (77) because the y velocity of the center of the hips is relatively constant within each step. Alternative models can be used in (52) for other choices of gait phasing variable.

7.2.2 Estimating Angular Momentum

When σ_i is estimated on the robot through

$$\hat{\sigma}_i = D_i(q)\hat{q},$$

where \hat{q} is estimated from encoder readings through numerical differentiation, the resulting signal presents non-physical behavior as detailed in Appendix D. Consequently, reduced-order Luenberger observers based on Luenberger (1966) are developed to estimate angular momentum in the frontal and sagittal planes.

Here, the reduced-order observer is derived for angular momentum in the frontal plane. We use a process similar to Grizzle et al. (2007), which was inspired by Menini and Tornambe (2002). A novel aspect here is that the reduced-order design is not carried out on the complete model of the robot, but instead on a simplified inverted pendulum model. The simplified model is based on the center of mass position of the full model, as shown in Figure 21, but does not include “flywheel-like” dynamics from individual-link velocities and momenta.

To start our reduced-order observer derivation, the dummy state η_{xz} and its derivative are defined as

$$\dot{\eta}_{xz} := \dot{\theta}_{xz} - L_{xz}\theta_{xz} \quad (54)$$

$$\ddot{\eta}_{xz} = \ddot{\theta}_{xz} - L_{xz}\dot{\theta}_{xz}, \quad (55)$$

where $L_{xz} > 0$ is a scalar to be chosen. From the inverted pendulum model, $\ddot{\theta}_{xz}$ in (55) is calculated as

$$\ddot{\theta}_{xz} = \frac{g}{l_{xz}} \sin(\theta_{xz}), \quad (56)$$

while (54) provides a substitution for $\dot{\theta}_{xz}$ in (55). Thus,

$$\dot{\eta}_{xz} = \frac{g}{l_{xz}} \sin(\theta_{xz}) - L_{xz}(\eta_{xz} + L_{xz}\theta_{xz}). \quad (57)$$

Using (57), the reduced-order observer for η_{xz} is defined as

$$\dot{\hat{\eta}}_{xz} := \frac{g}{l_{xz}} \sin(\theta_{xz}) - L_{xz}(\hat{\eta}_{xz} + L_{xz}\theta_{xz}). \quad (58)$$

Table 6. Indoor walking results from the first day of robot experiments. Terrain-disturbance profiles are created using the plywood boards shown in Figure 22. All results presented are first attempts. A “Success” indicates a successful crossing, and a blank space indicates that the control solution was not tested with that terrain profile.

Terrain Disturbance Profile (cm)			Control Solution			
			NHVC ₀	NHVC ₀ ^{Poincaré}	NHVC ₁	NHVC ₂
Flat Ground			Success	Lateral Fall	Success	Success
0 1.2 0			Success		Success	
0 1.2 2.6 1.2 0			Success		Success	
0 2.6 2.6 0			Success		Success	Success
0 3.8 3.8 0			Success		Success	
0 5.0 5.0 0			Success		Foot Slip	
0 1.2 2.6 3.8 6.7 7.9			Success			

At each impact, $\hat{\eta}_{xz}$ is updated to account for impact losses, which are calculated using the simplified model and (Westervelt et al. 2007, Eqn. (3.35)). Using (54) with (58), a subsequent observer for $\dot{\theta}_{xz}$ is defined as

$$\hat{\dot{\theta}}_{xz} := \hat{\eta}_{xz} + L_{xz}\theta_{xz}. \quad (59)$$

Using (59) and the simplified model, σ_{xz} and its derivatives are estimated as

$$\sigma_{xz,L} = M\ell_{xz}\hat{\dot{\theta}}_{xz} \quad (60)$$

$$\dot{\sigma}_{xz,L} = Mg\ell_{xz}\sin(\theta_{xz}) = \dot{\sigma}_{xz} \quad (61)$$

$$\ddot{\sigma}_{xz,L} = Mg\ell_{xz}\hat{\dot{\theta}}_{xz}\cos(\theta_{xz}), \quad (62)$$

where $\sigma_{xz,L}$ is the Luenberger-observer estimate of σ_{xz} , and an equivalent process yields $\sigma_{yz,L}$ to estimate σ_{yz} .

Remarks: (a) Because $\dot{\sigma}_{xz}$ is only dependent on the center of mass position and gravity, $\dot{\sigma}_{xz,L} = \dot{\sigma}_{xz}$ in (61). (b) As with $\bar{\sigma}_{xz}$, $\bar{\sigma}_{xz,L}$ for the robot implementation is found using (49). (c) In simulation, there is little difference between the Luenberger-observer angular momentum, σ_L , and the actual angular momentum, σ , as shown in Figure 28 in Appendix D.

7.3 Experiments

7.3.1 Indoor Experiments The first set of experiments with MARLO were performed indoors. As an initial robustness test of each control solution, terrain disturbances were created by either stacking sections of plywood boards in an organized fashion, as shown in Figure 22, or by throwing the boards randomly on the floor of the laboratory, as shown in Figure 23. Organized stacks of boards are immobile, quantifiable, and easily reproducible for each experiment. Randomly thrown boards, on the other hand, present the additional challenge of shifting under applied weight.

On the first attempt, MARLO traversed the length of the lab using the NHVC₀ control solution, and, subsequently, walked across various terrain obstacle courses. From the point where MARLO was started to the opposite wall is approximately 11 m. Each of the control solutions listed in Table 6 was tested in turn on the same day. With the exception of NHVC₀^{Poincaré}, each of them resulted in MARLO traversing the lab. Videos of experiments listed in Table 6 and random board experiments are available at Dynamic Legged Locomotion Lab (2016).

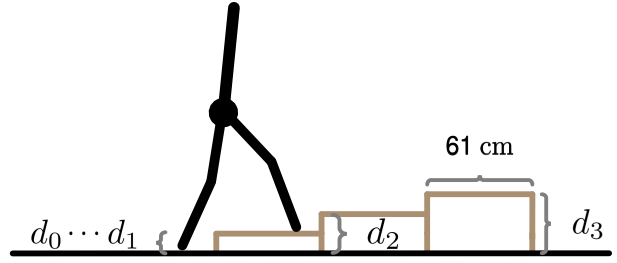


Figure 22. Sections of 61 cm-wide plywood boards are stacked to construct variable-height terrain disturbances.



Figure 23. MARLO walks over randomly thrown boards.

7.3.2 Outdoor Experiments For experiments outdoors, a mobile gantry was used to transport MARLO to locations within a 1 km radius of the laboratory and to catch MARLO in case of a fall or when experiments were terminated. As shown in Figure 24, the gantry does not provide external support of the robot during walking experiments. Power was supplied by a set of batteries carried by the gantry, which enabled MARLO to execute multiple experiments without returning to the lab for recharging. An Ethernet cable was

Table 7. Outdoor walking results for various terrains.

Control	Terrain Description	Forward Walking Speed (m/s)	MCOT (51)	COT		
				Liberal Estimate COT _{regen} (90)	Conservative Estimate COT _{abs.} (89)	P _{base} Component of COT
NHVC ₀	Concrete street, fairly flat with a slight lateral slope and some potholes.	0.92	0.65	0.64	1.13	0.23
NHVC ₃	Parking lot, fairly flat with a slight lateral slope.	0.90	0.67	0.62	1.19	0.24
NHVC ₋₃	Grass field, fairly flat.	0.95	0.68	0.65	1.16	0.22
NHVC ₃	Grass field using prosthetic feet, varying slope.	0.78	0.67	0.73	1.15	0.27
NHVC ₋₃	Gradual downhill with some lateral slope in parking lot.	0.98	0.68	0.57	1.22	0.22
NHVC ₃	Gradual uphill with consistent lateral slope on sidewalk.	0.91	0.69	0.69	1.16	0.23

**Figure 24.** MARLO walks gradually uphill with a MCOT of 0.69 and an average walking speed of 0.91 m/s.

sometimes used to download data after experiments; it is partially visible in the same figure.

MARLO under the control laws developed in this paper was able to traverse sloped sidewalks, parking lots, and grass fields. Outdoors, experiments were no longer limited by the 11 m indoor lab space. Table 7 examines results for a few of the outdoor experiments. Forward walking speed and MCOT (51) are calculated for each step, as detailed in Section 6.1, with averages provided in Table 7. Data for walking over a grass area were collected from 50 consecutive steps, whereas data for all other experiments were collected from 100 consecutive steps. Grass-field experiments lasted until the gantry was obstructed by outdoor terrain. Other experiments were manually shut down prior to MARLO

encountering an obstacle, with the exception of the downhill experiment, which ended due to an electrical-hardware malfunction. Figure 25 shows the step-to-step behavior of the robot induced by walking over naturally varying outdoor terrain. Videos of the outdoor experiments listed in Table 7 are available at Dynamic Legged Locomotion Lab (2016).

The cost of transport (COT) is an alternative metric to MCOT when evaluating locomotion efficiency. The methods used in the literature to estimate COT vary with hardware configuration of the robot being studied. In the strictest sense, COT should be assessed on the basis of the energy required to recharge batteries after traveling a known distance. When performing outdoor experiments with MARLO, the battery pack on the mobile-gantry was not configured to measure the supplied power. However, based on experiments in the lab with supply-power measurements, conservative and liberal estimates for COT, COT_{abs.} and COT_{regen} respectively, can be calculated using data that are also available during outdoor experiments. Both of these quantities are derived in Appendix E and included in Table 7. The P_{base} components of COT_{abs.} and COT_{regen} account for power used for MARLO's on-board sensing and computation.

7.4 Discussion of Experimental Results

The robot successfully traversed the lab, both with and without obstacles, using the same control algorithms tested in simulation and applied directly out of the optimization procedure described in Section 5.3. With the exception of NHVC₀^{Poincaré}, each of the control solutions yielded successful robot walking without any hand tuning. It is important to note that the actual robot differs significantly from the idealized control model. For example, the robot has estimated velocity signals for feedback control; varying levels of stiction and friction in each of the harmonic drives; series elastic actuators (springs in series with the motors in the sagittal plane and a timing belt in series with the motors in the frontal plane); a combination of manufactured and fatigued differences in individual physical components; and, due to on-going changes in hardware, an asymmetric mass distribution of 63 kg compared with the symmetric 55 kg simulation model. Despite these differences, the control solutions are sufficiently robust to handle the disturbances listed in Table 6 and randomly thrown piles of boards, as shown in Figure 23. On its first attempt, NHVC₀ traversed

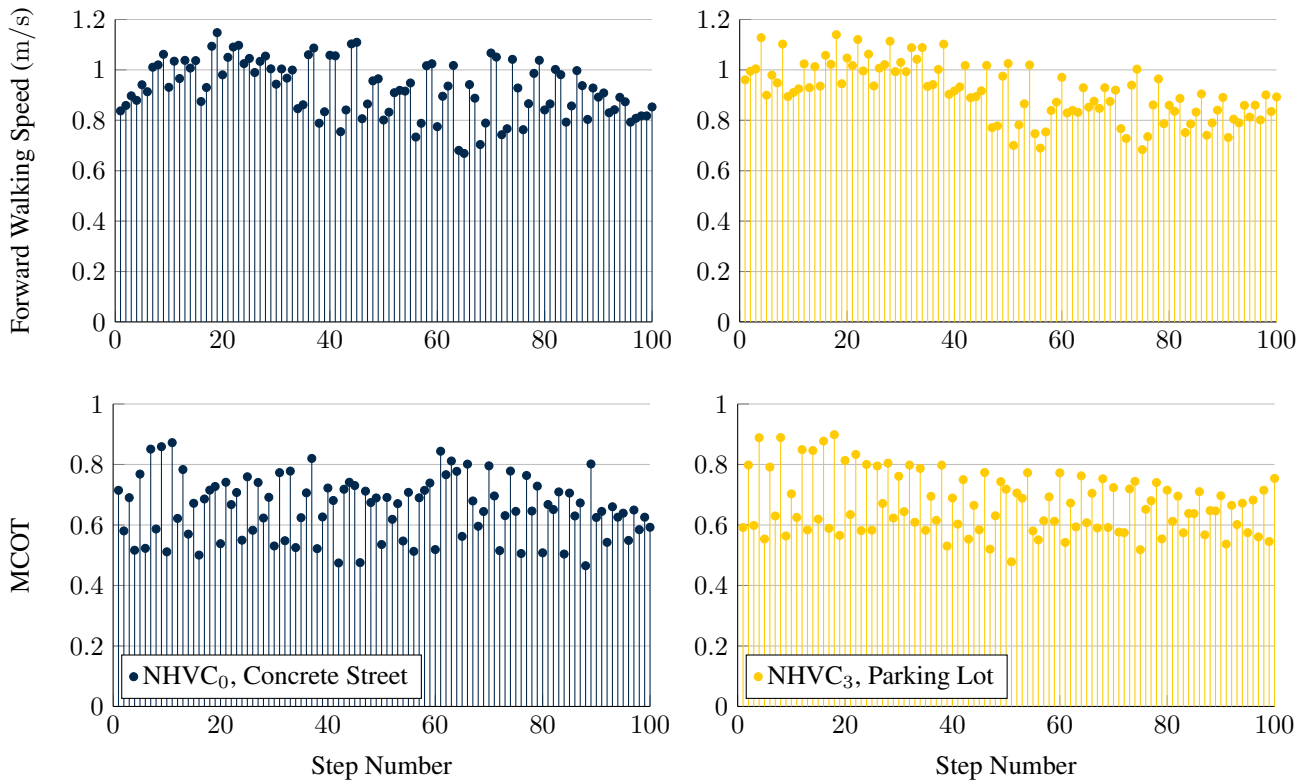


Figure 25. Step-to-step forward walking speed (top) and MCOT (bottom) during 100 consecutive steps of NHVC₀ on a concrete street (left) and NHVC₃ in a flat parking lot (right).

up and down 5 cm terrain disturbances—disturbances greater than those used during optimization.

After concluding indoor experiments, the NHVC₀ control solution was evaluated on the robot outdoors. MARLO walked for more than 100 steps across a slightly sloped paved area with potholes; the experiment was manually stopped to prevent the robot from colliding with a building. The MCOT was 0.65 and the forward walking speed was 0.92 m/s, as reported in Table 7. These values differ from the simulation values reported in Table 5 for at least two reasons: (1) because of differences between the simulation model and the physical robot mentioned previously and (2) because outdoor terrain injects additional step-to-step variability, as shown in Figure 25.

After observing how the NHVC₀ control solution performed outdoors, it became apparent that laterally-sloped terrain caused the most significant perturbation to the robot. A new control solution, NHVC₃, was optimized to address this type of disturbance and subsequently evaluated over a variety of terrains outdoors (see Table 7 for results).

Implementing NHVC₃ in multiple environments revealed many informative behaviors. First, the experiments with NHVC₃ show how COT_{abs} and COT_{regen} vary with terrain. For example, COT_{regen} is lower for downhill walking than for uphill walking. This is expected because walking downhill reduces the height of the robot's center of mass—a decrease in potential energy that may be recovered. Next, as shown in Table 7, the cost associated with P_{base} decreases with decreasing walking speed, consistent with the simulation work of Xi et al. (2015). Finally, the walking behavior of MARLO varies more with changes in hardware than

with changes in terrain. Switching to prosthetic feet in the grass field causes a greater change in walking speed than when traversing any other terrain with the normal hardware configuration.

Outdoor experiments with MARLO set a new precedent for walking efficiency in realistic environments. Figure 26 and Table 8 in Appendix E provide context for the outdoor walking experiments within the broader legged robotics literature. To the best of the authors' knowledge, MARLO under the NHVC₀ and NHVC₃ control solutions has achieved the lowest MCOT of any unsupported bipedal robot tested over rough terrain. Based on the conservative and liberal estimates of the COT in Table 7, it seems likely that this is also the case for the actual COT. In addition, this precedent is set at a faster speed than any other bipedal robot benchmark. Finally, whereas previous benchmarks have only been reported for treadmills and flat terrain, the NHVC₃ control solution provides a MCOT benchmark for walking over various realistic terrains.

8 Conclusions

A model-based control design methodology was developed for a class of underactuated 3D bipedal robots and evaluated both in simulations and in experiments. The first key aspect of the control design methodology was the computation of periodic orbits for walking that were robust to a finite set of perturbations. The second key aspect was the extension of the method of virtual constraints to include terms that depend on the robot's generalized velocity coordinates. Both aspects complement each other. Nonholonomic virtual

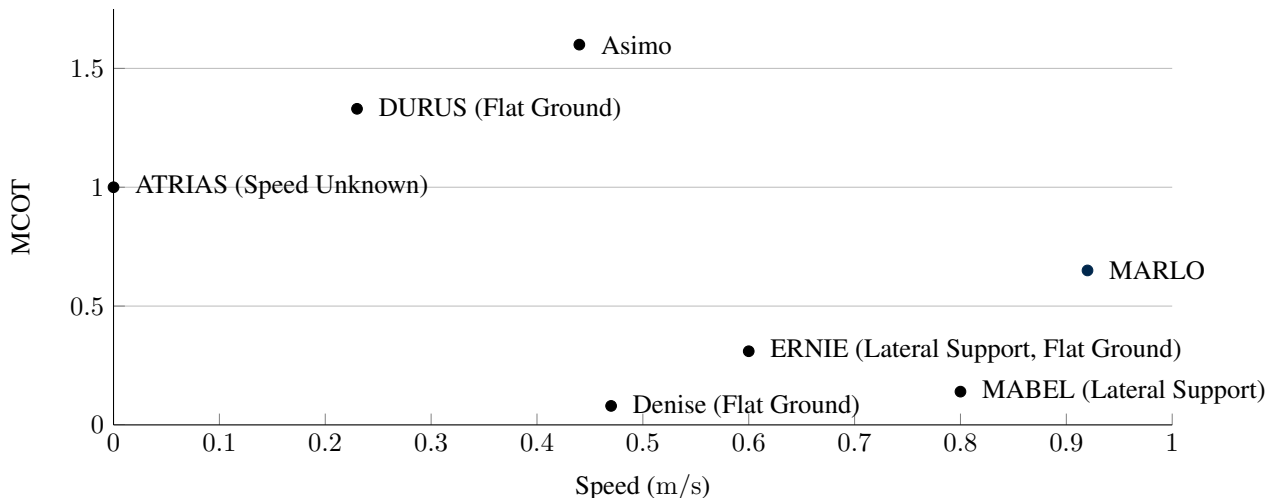


Figure 26. Mechanical cost of transport (MCOT) and speed for various bipedal robots. MARLO achieves the lowest MCOT of any unsupported bipedal robot tested over rough terrain (at a faster speed than any other bipedal benchmark). Cost of transport is used when MCOT is not available (see Table 8 in Appendix E for more details).

constraints enable the biped to adapt its posture with velocity, and the control optimization is performed while subjecting the biped model to disturbances that are representative of common failure modes. The result is an optimized walking controller that regulates velocity and, by extension, momentum in response to external disturbances, which addresses a characteristic failure mode of 3D bipedal robots.

The viability of the design methodology was illustrated on MARLO, a 3D bipedal robot with thirteen DOF in single support and six actuators. During indoor experiments across a relatively short (i.e., 11 m) section of a laboratory, the robot was able to walk on flat ground and over a series of obstacles without perception or a priori knowledge of the terrain. The controllers were designed on the basis of the full-order model of the robot and were implemented on the robot without hand tuning. Using the same design method during outdoor experiments, the robot traversed sloped sidewalks, parking lots, and grassy areas, while maintaining average walking speeds between 0.9–0.98 m/s.

The mechanical cost of transport was evaluated for a variety of terrain conditions. To the authors' knowledge, there is no precedent for this in the robotics literature, whether in simulation or in actual experiments. This evaluation is significant because, for practical applications, robots must be able to traverse a variety of environments in a reliable and efficient manner. It is hoped that other robotics researchers will consider environments other than flat ground when evaluating walking efficiency of their robots.

Future extensions of this work include perception and yaw control to enable navigation and obstacle avoidance.

Acknowledgements

Xingye Da, Omar Harib, and Ross Hartley are sincerely thanked for their contributions to the experiments. Hamed Razavi is thanked for discussions on inverted-pendulum models. Jonathan Hurst and his team at Oregon State University designed the robot.

Funding

This work was supported by the National Science Foundation (grant numbers ECCS-1343720 and ECCS-1231171).

Notes

1. A more comprehensive approach for calculating errors of perturbed trajectories that includes backward extensions of nominal trajectories is available in Saccoccia et al. (2014).
2. Unactuated yaw control methods for 3D bipeds with point feet are available in Shih et al. (2012); (Griffith 2016b, pp. 158).
3. A procedure for transforming a Lagrangian system with feedback control into a control-free Lagrangian system with a new class of trajectories is available in Shiriaev et al. (2014).
4. Because of limited actuation, selecting only the torso roll or the stance hip as a control variable causes the uncontrolled joint to drift during perturbations. However, a control variable defined by a combination of torso roll and stance hip causes the controller to respond to either component drifting, even if the exact behavior of each individual joint is no longer guaranteed in perturbed conditions. For the combined control variable in (43), the sign convention of the stance hip is selected such that an input from the hip actuator causes consistent directional output changes for both components.
5. In (50), we use the absolute Cartesian distance between the stance and swing feet at impact as the step length. Alternatively, step length can be defined as the y distance between the feet in the sagittal plane.

References

- Ackerman E (2015) Durus: Sri's ultra-efficient walking humanoid robot. URL <http://spectrum.ieee.org/automaton/robotics/humanoids/durus-sri-ultra-efficient-humanoid-robot>.
- Akbari Hamed K, Buss BG and Grizzle JW (2015) Exponentially stabilizing continuous-time controllers for periodic orbits of hybrid systems: Application to bipedal locomotion with ground height variations .
- Bhounsule PA, Cortell J, Grewal A, Hendriksen B, Karssen JD, Paul C and Ruina A (2014) Low-bandwidth reflex-based control for lower power walking: 65 km on a single battery charge. *The International Journal of Robotics Research* 33(10): 1305–1321.

- Bloch AM (2003) *Nonholonomic Mechanics and Control*. Springer-Verlag.
- Buss BG, Akbari Hamed K, Griffin BA and Grizzle JW (2016) Experimental results for 3d bipedal robot walking based on systematic optimization of virtual constraints. In: *American Control Conference*. Boston, MA, USA.
- Buss BG, Ramezani A, Akbari Hamed K, Griffin BA, Galloway KS and Grizzle JW (2014) Preliminary walking experiments with underactuated 3d bipedal robot marlo. In: *Intelligent Robots and Systems (IROS 2014), 2014 IEEE/RSJ International Conference on*. IEEE, pp. 2529–2536.
- Butterworth S (1930) On the theory of filter amplifiers. *Wireless Engineer* 7(6): 536–541.
- Byl K and Tedrake R (2009) Metastable walking machines. *The International Journal of Robotics Research* 28(8): 1040–1064.
- Chevallereau C, Grizzle J and Shih C (2009) Asymptotically stable walking of a five-link underactuated 3D bipedal robot. *IEEE Transactions on Robotics* 25(1): 37–50.
- Collins SH, Ruina A, Tedrake R and Wisse M (2005) Efficient bipedal robots based on passive-dynamic walkers. *Science* (307): 1082–1085.
- Dai H and Tedrake R (2012) Optimizing robust limit cycles for legged locomotion on unknown terrain. In: *Decision and Control (CDC), 2012 IEEE 51st Annual Conference on*. pp. 1207–1213.
- Dai H and Tedrake R (2013) L2-gain optimization for robust bipedal walking on unknown terrain. In: *Robotics and Automation (ICRA), 2013 IEEE International Conference on*.
- Dynamic Legged Locomotion Lab (2016) Nonholonomic virtual constraints and gait optimization for robust walking control. URL <https://youtu.be/81I0H5d0tUM>.
- Gregg RD, Lenzi T, Hargrove LJ and Sensinger JW (2014a) Virtual constraint control of a powered prosthetic leg: From simulation to experiments with transfemoral amputees. *IEEE Transactions on Robotics*.
- Gregg RD, Rouse EJ, Hargrove LJ and Sensinger JW (2014b) Evidence for a time-invariant phase variable in human ankle control. *PLoS ONE* 9: 1–13.
- Griffin B (2016a) code for 3d control design and simulation. URL <http://www.griffb.com/publications/>.
- Griffin B (2016b) *Nonholonomic Virtual Constraints and Gait Optimization for Robust Robot Walking Control*. PhD Thesis, University of Michigan.
- Griffin B and Grizzle J (2015a) Nonholonomic virtual constraints for dynamic walking. In: *IEEE Conf. on Decision and Control*. pp. 4053–4060.
- Griffin B and Grizzle J (2015b) Walking gait optimization for accommodation of unknown terrain height variations. In: *American Control Conference (ACC), 2015*. Chicago, IL, USA, pp. 4810–4817.
- Grimes J and Hurst J (2012) The design of ATRIAS 1.0 a unique monopod, hopping robot. *Climbing and walking Robots and the Support Technologies for Mobile Machines, International Conference on*.
- Grizzle JW, Abba G and Plestan F (2001) Asymptotically stable walking for biped robots: Analysis via systems with impulse effects. *IEEE Transactions on Automatic Control* 46: 51–64.
- Grizzle JW, Choi JH, Hammouri H and Morris B (2007) On observer-based feedback stabilization of periodic orbits in bipedal locomotion. In: *Proceedings of Methods and Models in Automation and Robotics (MMAR 2007)*. Szczecin, Poland.
- Hamed KA and Grizzle JW (2014) Event-based stabilization of periodic orbits for underactuated 3-d bipedal robots with left-right symmetry. *IEEE Transactions on Robotics* 30(2): 365–381.
- Hereid A, Cousineau EA, Hubicki CM and Ames AD (2016) 3d dynamic walking with underactuated humanoid robots: A direct collocation framework for optimizing hybrid zero dynamics. In: *IEEE International Conference on Robotics and Automation*. Stockholm, Sweden.
- Hobbeln DG and Wisse M (2008a) Ankle actuation for limit cycle walkers. *The International Journal of Robotics Research* 27(6): 709–735.
- Hobbeln DGE and Wisse M (2007) A disturbance rejection measure for limit cycle walkers: The gait sensitivity norm. *Robotics, IEEE Transactions on* 23(6): 1213–1224.
- Hobbeln DGE and Wisse M (2008b) Swing-leg retraction for limit cycle walkers improves disturbance rejection. *Robotics, IEEE Transactions on* 24(2): 377–389.
- Hürmüzlü Y and Marghitu DB (1994) Rigid body collisions of planar kinematic chains with multiple contact points. *International Journal of Robotics Research* 13(1): 82–92.
- Hurst J (2015) Ri seminar: Designing robots to walk and run. URL <https://www.youtube.com/watch?v=2NvFymqa8qY>.
- Hyun DJ, Seok S, Lee J and Kim S (2014) High speed trot-running: Implementation of a hierarchical controller using proprioceptive impedance control on the mit cheetah. *The International Journal of Robotics Research* 33(11): 1417–1445.
- Isidori A (1995) *Nonlinear Control Systems*. Third edition. Berlin: Springer-Verlag.
- Kajita S, Yamaura T and Kobayashi A (1992) Dynamic walking control of biped robot along a potential energy conserving orbit. *IEEE Transactions on Robotics and Automation* 8(4): 431–37.
- Kolathaya S and Ames AD (2012) Achieving bipedal locomotion on rough terrain through human-inspired control. In: *Safety, Security, and Rescue Robotics (SSRR), 2012 IEEE International Symposium on*. IEEE, pp. 1–6.
- Kong FH, Boudali AM and Manchester IR (2015) Phase-indexed ilc for control of underactuated walking robots. In: *2015 IEEE Conference on Control Applications (CCA)*. pp. 1467–1472.
- Kooleen T, de Boer T, Rebula J, Goswami A and Pratt J (2012) Capturability-based analysis and control of legged locomotion, Part 1: Theory and application to three simple gait models. *The International Journal of Robotics Research* 31(9): 1094–1113.
- Kuo AD (1999) Stabilization of lateral motion in passive dynamic walking. *International Journal of Robotics Research* 18(9): 917–930.
- Luenberger D (1966) Observers for multivariable systems. *IEEE Transactions on Automatic Control* 11(2): 190–197.
- Manchester IR, Mettin U, Iida F and Tedrake R (2011) Stable dynamic walking over uneven terrain. *The International Journal of Robotics Research* : 265–279.
- Manchester IR and Umenberger J (2014) Real-time planning with primitives for dynamic walking over uneven terrain. In: *2014 IEEE International Conference on Robotics and Automation*

- (ICRA). pp. 4639–4646.
- Martin AE, Post DC and Schmiedeler JP (2014a) Design and experimental implementation of a hybrid zero dynamics-based controller for planar bipeds with curved feet. *The International Journal of Robotics Research* 33(7): 988–1005.
- Martin AE, Post DC and Schmiedeler JP (2014b) The effects of foot geometric properties on the gait of planar bipeds walking under HZD-based control. *The International Journal of Robotics Research* 33(12): 1530–1543.
- Menini L and Tornambe A (2002) Reduced-order observers for the velocity estimation of nonlinear mechanical systems subject to non-smooth impacts. In: *American Control Conference*. pp. 2639–2644.
- Oregon State DRL (2015) Atrias robot: Battery drain. URL <https://www.youtube.com/watch?v=seOnSJMZKcY>.
- Park H, Ramezani A and Grizzle JW (2013) A finite-state machine for accommodating unexpected large ground height variations in bipedal robot walking. *IEEE Transactions on Robotics* 29(29): 331–345.
- Park HW, Wensing P and Kim S (2015) Autonomous running jumps over obstacles in the mit cheetah 2. URL https://www.youtube.com/watch?v=_luhn7TLfWU.
- Post DC and Schmiedeler JP (2014) Velocity disturbance rejection for planar bipeds walking with hzd-based control. In: *2014 IEEE/RSJ International Conference on Intelligent Robots and Systems*. pp. 4882–4887.
- Pratt J, Koolen T, de Boer T, Rebula J, Cotton S, Carff J, Johnson M and Neuhaus P (2012) Capturability-based analysis and control of legged locomotion, Part 2: Application to M2V2, a lower-body humanoid. *The International Journal of Robotics Research* 31(10): 1117–1133.
- Pratt J and Tedrake R (2006) Velocity-based stability margins for fast bipedal walking. In: Diehl M and Mombaur K (eds.) *Fast Motions in Biomechanics and Robotics, Lecture Notes in Control and Information Sciences*, volume 340. Springer Berlin Heidelberg. ISBN 978-3-540-36118-3, pp. 299–324.
- Ramezani A, Hurst JW, Akbari Hamed K and Grizzle JW (2014) Performance Analysis and Feedback Control of ATRIAS, A Three-Dimensional Bipedal Robot. *Journal of Dynamic Systems, Measurement, and Control* 136(2).
- Razavi H, Bloch AM, Chevallereau C and Grizzle JW (2015) Restricted discrete invariance and self-synchronization for stable walking of bipedal robots. In: *2015 American Control Conference (ACC)*. pp. 4818–4824.
- Saccon A, van de Wouw N and Nijmeijer H (2014) Sensitivity analysis of hybrid systems with state jumps with application to trajectory tracking. In: *Decision and Control (CDC), 2014 IEEE 53rd Annual Conference on*. pp. 3065–3070.
- Saglam CO and Byl K (2014a) Quantifying the trade-offs between stability versus energy use for underactuated biped walking. In: *IEEE/RSJ Conference on Intelligent Systems and Robots*. IEEE.
- Saglam CO and Byl K (2014b) Robust policies via meshing for metastable rough terrain walking. In: *Proceedings of Robotics: Science and Systems*. Berkeley, USA.
- Seok S, Wang A, Chuah MY, Otten D, Lang J and Kim S (2013) Design principles for highly efficient quadrupeds and implementation on the mit cheetah robot. In: *Robotics and Automation (ICRA), 2013 IEEE International Conference on*. IEEE, pp. 3307–3312.
- Seyfarth A, Geyer H and Herr H (2003) Swing leg retraction: A simple control model for stable running. *Journal of Experimental Biology* 206: 2547–2555.
- Shih CL, Grizzle J and Chevallereau C (2012) From Stable Walking to Steering of a 3D Bipedal Robot with Passive Point Feet. *Robotica* 30(07): 1119–1130.
- Shiriaev AS, Freidovich LB and Spong MW (2014) Controlled invariants and trajectory planning for underactuated mechanical systems. *Automatic Control, IEEE Transactions on* 59(9): 2555–2561.
- Sreenath K, Park HW, Poulakakis I and Grizzle JW (2011) A compliant hybrid zero dynamics controller for stable, efficient and fast bipedal walking on mabel. *The International Journal of Robotics Research* 30(9): 1170–1193.
- Westervelt ER, Buche G and Grizzle JW (2004) Experimental validation of a framework for the design of controllers that induce stable walking in planar bipeds. *International Journal of Robotics Research* 24(6): 559–582.
- Westervelt ER, Grizzle JW, Chevallereau C, Choi J and Morris B (2007) *Feedback Control of Dynamic Bipedal Robot Locomotion*. Control and Automation. Boca Raton, FL: CRC Press.
- Westervelt ER, Grizzle JW and Koditschek DE (2003) Hybrid zero dynamics of planar biped walkers. *IEEE Transactions on Automatic Control* 48(1): 42–56.
- Wisse M, Feliksdal G, Van Frankenhuyzen J and Moyer B (2007) Passive-based walking robot. *Robotics & Automation Magazine, IEEE* 14(2): 52–62.
- Wisse M, Schwab AL, van der Linde RQ and van der Helm FCT (2005) How to keep from falling forward: Elementary swing leg action for passive dynamic walkers. *IEEE Trans. on Robotics* 21(3): 393–401.
- Xi W, Yesilevskiy Y and Remy CD (2015) Selecting gaits for economical locomotion of legged robots. *The International Journal of Robotics Research* .
- Yang T, Westervelt E, Serrani A and Schmiedeler JP (2009) A framework for the control of stable aperiodic walking in underactuated planar bipeds. *Autonomous Robots* 27(3): 277–290.
- Zhao H, Ma W, Ames A and Zeagler M (2014) Human-inspired multi-contact locomotion with AMBER2. In: *Cyber-Physical Systems (ICCPs), 2014 ACM/IEEE International Conference on*. pp. 199–210.

Appendix A: Extended Model for Invariant Hybrid Zero Dynamics

Parameters κ are used to achieve invariance of the *zero dynamics* manifold induced by output vector y (37). If a hybrid system is invariant to the zero dynamics manifold, *hybrid zero dynamics* are achieved (see also Appendix B). For the choice of output in (48), it is straightforward to construct a function $\Psi : \mathcal{S}^d \times \mathcal{B} \rightarrow \mathcal{K}$ such that for all

$$\beta \in \mathcal{B} \text{ and } \begin{bmatrix} q^+ \\ \dot{q}^+ \end{bmatrix} = \Delta(q^-, \dot{q}^-)$$

the initial values of the outputs are zeroed, that is,

$$\begin{bmatrix} 0 \\ 0 \end{bmatrix} = \begin{bmatrix} y^+ \\ \dot{y}^+ \end{bmatrix} = \begin{bmatrix} h(q^+, \sigma^+, \kappa^+, \beta) \\ \frac{\partial}{\partial q} h(q^+, \sigma^+, \kappa^+, \beta) \dot{q}^+ + \frac{\partial}{\partial \sigma} h(q^+, \sigma^+, \kappa^+, \beta) \dot{\sigma}^+ \end{bmatrix} \quad (63)$$

for $\kappa^+ = \Psi(q^-, \dot{q}^-, \beta)$. The current implementation of κ^+ is derived in Appendix B.

Parameters κ are constant within each step and are reset at the end of each step, hence, they are included as states in the dynamics with

$$x_e := [q, \dot{q}, \kappa]' \quad (64)$$

and $\dot{\kappa} = 0$. The extended closed-loop model used is then

$$\Sigma : \begin{cases} \dot{x}_e = f^{cl}(x_e, \beta) & x_e^- \notin \mathcal{S}_e^d \\ x_e^+ = \Delta_e(x_e^-) & x_e^- \in \mathcal{S}_e^d, \end{cases} \quad (65)$$

where

$$f^{cl}(x_e, \beta) = f^{cl}(x, \kappa, \beta) := \begin{bmatrix} f(x) + g(x)\Gamma(x, \kappa, \beta) \\ 0 \end{bmatrix}, \quad (66)$$

$$\Delta_e(x_e^-, \beta) := \begin{bmatrix} \Delta(q^-, \dot{q}^-) \\ \Psi(q^-, \dot{q}^-, \beta) \end{bmatrix}, \quad (67)$$

and

$$\mathcal{S}_e^d := \mathcal{S}^d \times \mathcal{K}. \quad (68)$$

Remarks: (a) Because $\kappa^+ = \Psi(q^-, \dot{q}^-, \beta)$, (63) is independent of the current value of κ . (b) Because of the second-order system (41) and the reset map in (63), solutions of (66) that are initialized in \mathcal{S}_e^d satisfy $y(t) \equiv 0$. This has two consequences: (i) The solutions evolve on the zero dynamics manifold. (ii) The feedback term u_{fb} in (39) is identically zero, and thus Γ in (40) is independent of the gains K_p and K_d .

Appendix B: Bézier Parameter Reset Derivation

When swapping stance legs in periodic or perturbed conditions (e.g., walking over terrain disturbances), control parameters κ must be reset such that post-impact outputs are zeroed in (63). Using output vector y (37), choice of output h (42), and desired evolution of controlled outputs h_d (44), output terms dependent on κ are defined as

$$h_\kappa(\tau(q), \alpha(\kappa, \beta)) := h_{d,\tau}(\tau(q), \kappa, \beta) \quad (69)$$

and output terms independent of κ are defined as

$$h_\beta(q, \sigma, \beta) := h_0(q, \beta) - h_{d,\sigma}(\sigma, \beta). \quad (70)$$

Next, h_κ and h_β substitute into (37) as

$$y = h_\beta(q, \sigma, \beta) - h_\kappa(\tau(q), \alpha(\kappa, \beta)). \quad (71)$$

From (71) and $h_{d,\tau,i}$ (45), we find that the desired trajectory of h_β along τ is specified by Bézier parameters $\alpha(\kappa, \beta) \in \mathbb{R}^{6 \times (M+1)}$, which are defined as

$$\alpha(\kappa, \beta) := [\alpha_0(\kappa), \alpha_1(\kappa), \alpha_2(\beta), \dots, \alpha_M(\beta)]. \quad (72)$$

It is evident from (45) that $\alpha_0(\kappa)$ and $\alpha_1(\kappa)$ have the most effect on trajectories during low τ values immediately after impact. The remaining columns of $\alpha(\kappa, \beta)$, defined by fixed parameters β , determine trajectories toward the end of the gait. Hence, perturbed trajectories return to the nominal gait as τ increases.

Let $y^+ = \dot{y}^+ = 0$ as in (63). Using (71), this implies that

$$h_\kappa(\tau(q^+), \alpha(\kappa^+, \beta)) = h_\beta(q^+, \sigma^+, \beta), \quad (73)$$

or simply $h_\kappa(\tau^+, \kappa^+, \beta) = h_\beta^+$. To satisfy (73), we must reset at least one column of Bézier parameters, $\alpha_0(\kappa^+)$. To guarantee desired trajectories match post-impact velocities, we reset a second column, $\alpha_1(\kappa^+)$, to satisfy

$$\frac{\partial h_\kappa(\tau^+, \kappa^+, \beta)}{\partial \tau} \dot{\tau}^+ = \dot{h}_\beta^+. \quad (74)$$

Using (69), (45), and (72), we solve for $\alpha_0(\kappa^+)$ and $\alpha_1(\kappa^+)$ in (73) and (74) as

$$\alpha_0(\kappa^+) = \frac{h_\beta^+ - \sum_{k=1}^M \alpha_k \frac{M! (\tau^+)^k (1-\tau^+)^{M-k}}{k! (M-k)!}}{(1-\tau^+)^M} \quad (75)$$

$$\alpha_1(\kappa^+) = \frac{\dot{h}_\beta^+ - \alpha_2 M(M-1) \tau^+ (1-\tau^+)^{M-2} - a + b}{M((1-\tau^+)^{M-1} + \tau^+ (1-\tau^+)^{M-2})}, \quad (76)$$

where $a = \sum_{k=2}^{M-1} (\alpha_{k+1} - \alpha_k) \frac{M! (\tau^+)^k (1-\tau^+)^{M-1-k}}{k! (M-1-k)!}$ and $b = \frac{M}{1-\tau^+} \left(h_\beta^+ - \sum_{k=2}^M \alpha_k \frac{M! (\tau^+)^k (1-\tau^+)^{M-k}}{k! (M-k)!} \right)$. (75) and (76) are a solution for $\kappa^+ = \Psi(q^-, \dot{q}^-, \beta)$ that always satisfies (63).

Appendix C: Extended Gait Phasing Variable and Bézier Polynomials

Along periodic walking gaits, the y position of the center of the hips, $p_{HIP,y}$ shown in Figure 6, is monotonic and cycles between a minimum value, $p_{HIP,y}^{min}$, and a maximum value, $p_{HIP,y}^{max}$. The nominal gait phasing variable is defined as

$$\tau(q) := \frac{p_{HIP,y} - p_{HIP,y}^{min}}{p_{HIP,y}^{max} - p_{HIP,y}^{min}}, \quad (77)$$

where $p_{HIP,y}^{min}$ is the initial value of $p_{HIP,y}$ each step, and $p_{HIP,y}^{max}$ is the final value of $p_{HIP,y}$ on the periodic orbit.

If the periodic orbit is exited and $\tau(q) > 1$, the desired trajectory defined by the nominal gait phasing variable and Bézier polynomials can become counterproductive. To avoid this, an alternative trajectory is defined using an extended gait phasing variable,

$$\tau_{ext}(q) := \frac{p_{HIP,y} - p_{HIP,y}^{max}}{p_{HIP,y}^{max} - p_{HIP,y}^{min}}, \quad (78)$$

and a second set of Bézier polynomials, $\alpha_{ext}(\beta)$. Note that (77) subtracts $p_{HIP,y}^{min}$ in the numerator, whereas (78) subtracts $p_{HIP,y}^{max}$. The transition between (77) and (78) occurs when $\tau(q) = 1$, which means $p_{HIP,y}(q) = p_{HIP,y}^{max}$.

and $\tau_{ext}(q) = 0$. The complete $\bar{\tau}(q)$ and $\bar{\alpha}(\kappa, \beta)$ used in (45) are defined using their nominal definitions and equivalent extensions as

$$\bar{\tau}(q) := \begin{cases} \tau(q) & \text{if } p_{HIP,y}(q) \leq p_{HIP,y}^{max} \\ \tau_{ext}(q) & \text{if } p_{HIP,y}(q) > p_{HIP,y}^{max} \end{cases} \quad (79)$$

$$\bar{\alpha}(\kappa, \beta) := \begin{cases} \alpha(\kappa, \beta) & \text{if } p_{HIP,y}(q) \leq p_{HIP,y}^{max} \\ \alpha_{ext}(\beta) & \text{if } p_{HIP,y}(q) > p_{HIP,y}^{max} \end{cases}. \quad (80)$$

$\tau(q)$, $\tau_{ext}(q)$, $\alpha(\kappa, \beta)$, and $\alpha_{ext}(\beta)$ should be defined such that (45) is continuous. One way of achieving continuity is by defining τ_{ext} such that $\{(q, \dot{q})' \in \mathcal{X} \mid \tau(q) = 1\}$

$$\tau_{ext}(q) = 0 \quad (81)$$

$$\dot{\tau}_{ext}(q, \dot{q}) = \dot{\tau}(q, \dot{q}), \quad (82)$$

and defining α_{ext} such that

$$\alpha_{ext,0} = \alpha_M \quad (83)$$

$$\alpha_{ext,1} = \alpha_{ext,0} + (\alpha_M - \alpha_{(M-1)}) \frac{M}{M_{ext}}, \quad (84)$$

where α_i and $\alpha_{ext,i}$ are the $(i+1)$ columns of α and α_{ext} , and $(M+1)$ and $(M_{ext}+1)$ are the degree of Bézier polynomials associated with α and α_{ext} . Using (83) and (84), the complete extended Bézier parameters $\alpha_{ext}(\beta) \in \mathbb{R}^{6 \times (M_{ext}+1)}$ are defined as

$$\alpha_{ext}(\beta) := [\alpha_{ext,0}, \alpha_{ext,1}, \alpha_{ext,2}(\beta), \dots, \alpha_{ext,M_{ext}}(\beta)], \quad (85)$$

where $\alpha_{ext,2}(\beta), \dots, \alpha_{ext,M_{ext}}(\beta)$ are found in optimization.

Remarks: (a) If $M \neq M_{ext}$, M_{ext} replaces M in $h_{d,\tau,i}$ (45) when using the extended parameters. (b) Defining $\tau(q)$, $\tau_{ext}(q)$, $\alpha(\kappa, \beta)$, and $\alpha_{ext}(\beta)$ such that control trajectories defined by (45) are continuous does not guarantee continuity of control inputs u in (40). This is evident in Figure 19 where, when $\tau > 1$ (i.e., during downhill walking), the extended controller causes a jump in u that immediately requires a greater friction coefficient.

Appendix D: Comparison of Original and Processed Signals

The phase estimator, $\hat{\tau}$ in Figure 27, and Luenberger-observer angular momentum, σ_L in Figure 28, are compared with their corresponding original signals. Signal data are collected from simulation and the robot implementation. Simulation data corresponds to two steps from the periodic orbit of NHVC₀. Robot experiment data are taken from two steps using the NHVC₀ control solution. Angular momentum and other velocity-based quantities generally decrease at step transition due to impact losses.

For robot experiments, the original signals for $\dot{\tau}$, σ_{xz} , and σ_{yz} use velocities \hat{q} that are estimated from encoder readings through numerical differentiation, which presents non-physical behavior. This non-physical behavior is evident in $\dot{\tau}$ directly following impacts (see Figure 27) and is evident in σ_{xz} and σ_{yz} throughout the entire step (see Figure 28). In all cases, signal oscillations are caused by \hat{q} , not physical oscillations on the robot (see videos of experiments at Dynamic Legged Locomotion Lab (2016)). Consequently,

original signals for $\dot{\tau}$, σ_{xz} , and σ_{yz} are replaced with signals $\dot{\hat{\tau}}$, $\sigma_{xz,L}$, and $\sigma_{yz,L}$, which track well with the original signals in simulation and provide reliable estimates during robot experiments.

Appendix E: Cost of Transport Derivation

The cost of transport (COT) is an alternative metric to the mechanical cost of transport (MCOT) for evaluating locomotion efficiency. Table 8 provides a review of the MCOT and COT for various legged robots. Here, we make the distinction between COT calculated instantaneously as

$$\text{COT}_P := \frac{P}{Mgv_y}, \quad (86)$$

where M is the total mass of the biped, g is the acceleration due to gravity, and P is power consumption at forward velocity v_y , and COT calculated over a period of time as

$$\text{COT} := \frac{E}{Mgd_y}, \quad (87)$$

where E is the energy used to travel distance d_y . (87) is more useful to the current work than (86), because it accounts for local changes that occur for non-periodic conditions, such as when traversing almost any outdoor environment.

Based on experiments in the lab with supply-power measurements, a conservative estimate for COT can be calculated using data that is also available during outdoor experiments. The conservative estimate uses the absolute MCOT, calculated as

$$\text{MCOT}_{\text{abs.}} := \frac{1}{Mgd_y} \int_0^{T_0} \sum_{i=1}^6 |u_i \dot{q}_{m,i}| dt, \quad (88)$$

which includes negative actuator work, as in (Hobbelink and Wisse 2008a, Eqn. (4)). As in (Xi et al. 2015, Eqn. (23)), a fixed power cost, P_{base} , is added to account for ancillary electronics. Based on the highest measurement for power consumption of on-board sensing and computation on MARLO, $P_{\text{base}} = 131.7$ W. The resulting conservative estimate for COT is defined as

$$\text{COT}_{\text{abs.}} := \frac{1}{Mgd_y} \int_0^{T_0} P_{\text{base}} + \sum_{i=1}^6 |u_i \dot{q}_{m,i}| dt, \quad (89)$$

which is consistently higher than the actual measured power consumption, because it does not consider any negative-work regenerative capabilities of the amplifiers and batteries.

For comparison, a liberal estimate based on the regenerative COT is defined as

$$\text{COT}_{\text{regen}} := \frac{1}{Mgd_y} \int_0^{T_0} P_{\text{base}} + \sum_{i=1}^6 u_i \dot{q}_{m,i} dt, \quad (90)$$

which is consistently lower than the actual measured power consumption due to regenerative losses in hardware. Based on power experiments with nominal periodic motion, the average power consumption based on (89) is about 14% higher than the actual measured values, while the average power consumption based on (90) is about 30% lower.

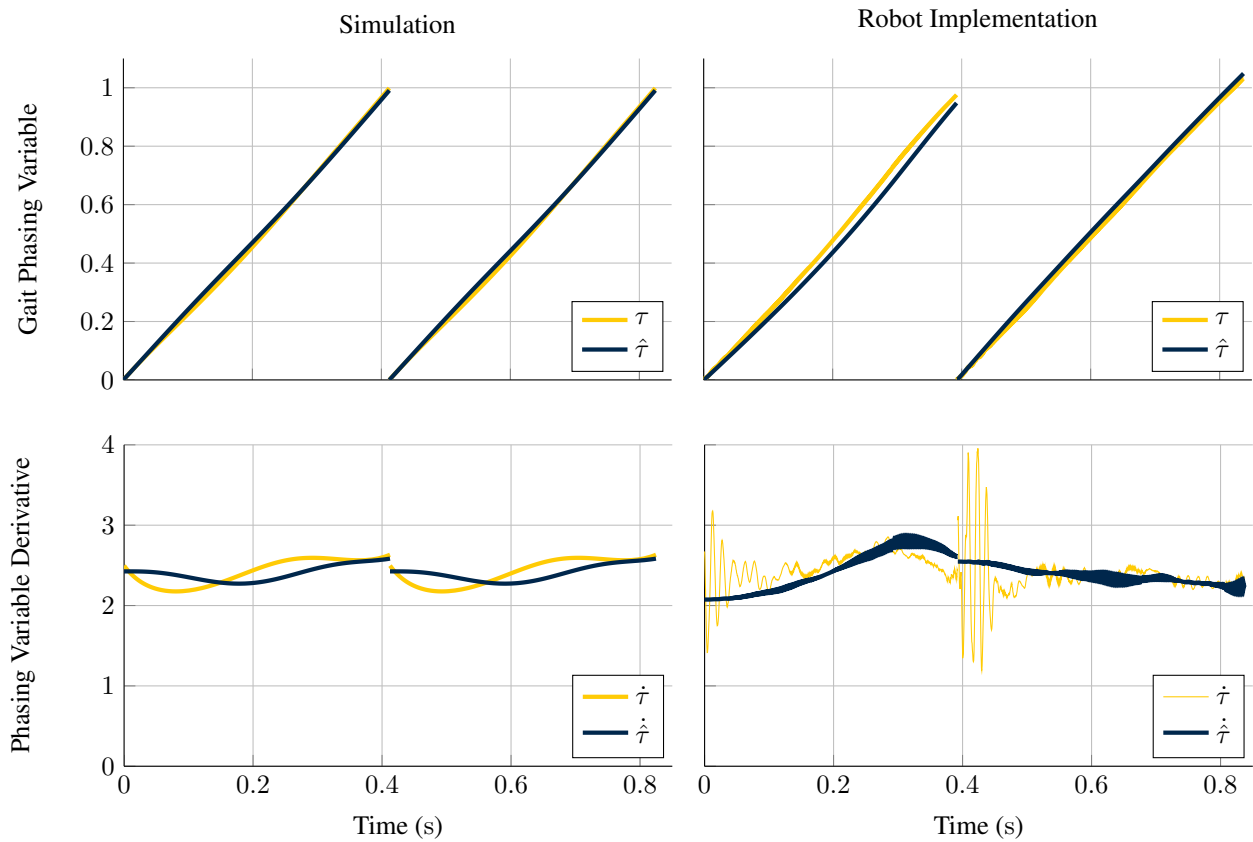


Figure 27. Comparison of the gait phasing variable (τ) and the phase estimator ($\hat{\tau}$) in simulation (left) and on the robot (right).

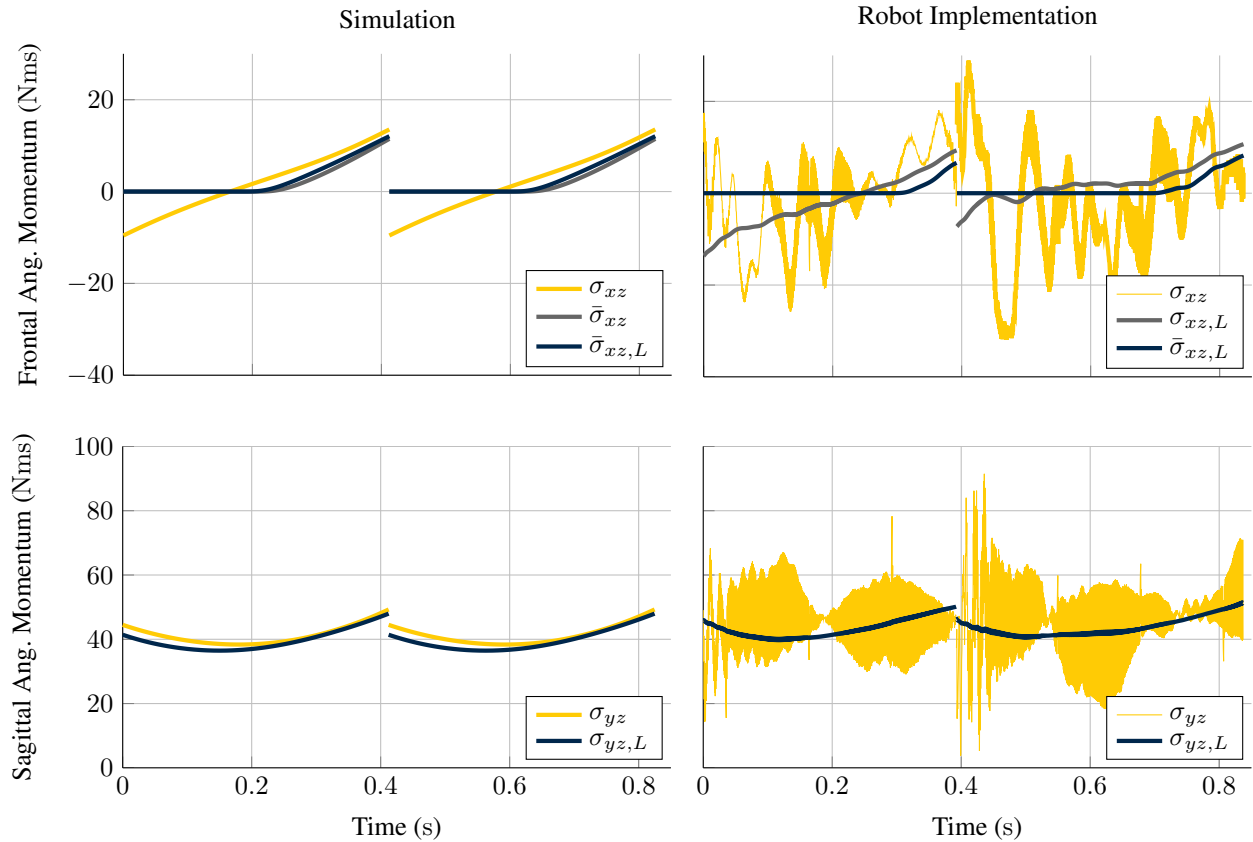


Figure 28. Comparison of angular momentum (σ) and the Luenberger-observer angular momentum (σ_L) in the frontal (top) and sagittal (bottom) planes, in simulation (left) and on the robot (right). The sign convention of σ_{xz} alternates between left and right stance for symmetric control. $\bar{\sigma}_{xz}$ and $\bar{\sigma}_{xz,L}$ are found using (49).

Table 8. Mechanical cost of transport and cost of transport for various legged robots. Blank spaces indicate that information is not currently available.

Robot	MCOT	COT	Configuration for Cost of Transport Calculation							Rough Terrain Tested
			Speed (m/s)	Mass (kg)	Legs	Lateral Support	Includes Abduction Motors	On-board Power	Test Terrain	
Ranger (COT record) Bhounsule et al. (2014)	0.04	0.19		9.9	4	No	N/A	Yes	Linoleum Floor	No
Human (estimated) Collins et al. (2005)	0.05	0.2			2	No				Yes
Ranger (distance record) Bhounsule et al. (2014)		0.28	0.59	9.9	4	No	N/A	Yes	Indoor Track	No
Denise Collins et al. (2005) Wisse et al. (2007)	0.08		0.47	8	2	No	N/A	Yes		No
Meta	0.09 ^a		0.4	12.3	4	No	N/A	Yes		Yes
MIT Cheetah Hyun et al. (2014) Seok et al. (2013)		0.5	6	33	4	Yes	No	No	Treadmill	No ^b
MABEL Sreenath et al. (2011) Park et al. (2013)	0.14		0.8	58	2	Yes	N/A	No	Flat	Yes
ERNIE	0.31 ^c		0.60	19.6	2	Yes	N/A	No	Flat	No
MARLO (NHVC ₀) (current work)	0.65		0.92	63	2	No	Yes	No ^d	Concrete Street	Yes
MARLO (NHVC ₃) (current work)	0.68		0.95	63	2	No	Yes	No	Grass Field	Yes
MARLO (NHVC ₃) (current work)	0.69		0.91	63	2	No	Yes	No	Gradual Uphill	Yes
ATRIAS (OSU) Hurst (2015)		1.0			2	No	Yes	Yes		Yes
DURUS (DRC) Hereid et al. (2016) Ackerman (2015)		1.33	0.23	80	2	No	Yes	Yes	Treadmill	No
Asimo (estimated) Collins et al. (2005)	1.6	3.2	0.44	52	2	No	Yes	Yes		Yes
ATLAS (estimated) Ackerman (2015)		20		157	2	No	Yes	Yes		Yes

^aCalculated using the absolute mechanical power (see (Hobbelin and Wisse 2008a, Eqn. (4))).

^bThe MIT Cheetah II has performed jumps over obstacles and outdoor running, but no COT information is available (see Park et al. (2015)).

^cCalculated using the absolute mechanical power (see (Post and Schmiedeler 2014, Eqn. (12))).

^dMARLO can be configured to use an on-board 3 kg battery for power (see Oregon State DRL (2015)).